

<sup>1</sup>  
<sup>2</sup> Susceptible host dynamics explain pathogen resilience to  
<sup>3</sup> perturbations

<sup>4</sup>  
<sup>5</sup> Sang Woo Park, . . . , Bryan T. Grenfell, Sarah Cobey

## <sup>6</sup> Abstract

<sup>7</sup> Major priority for epidemiological research in the time of anthropogenic change is un-  
<sup>8</sup> derstanding how infectious disease dynamics respond to perturbations. Interventions  
<sup>9</sup> to slow the spread of SARS-CoV-2 significantly disrupted the transmission of other  
<sup>10</sup> human pathogens. As interventions lifted, whether and when respiratory pathogens  
<sup>11</sup> would eventually return to their pre-pandemic dynamics remains to be answered. We  
<sup>12</sup> develop a framework for estimating pathogen resilience based on how fast epidemic  
<sup>13</sup> patterns return to their pre-pandemic, endemic dynamics. Our analysis suggests  
<sup>14</sup> that some pathogens may have settled to endemic cycles that are different from their  
<sup>15</sup> pre-pandemic patterns. Finally, we show that the replenishment rate of the suscep-  
<sup>16</sup> tible pool is a key determinant of pathogen resilience. Our framework offers a novel  
<sup>17</sup> perspective to characterizing the dynamics of endemic pathogens and their responses  
<sup>18</sup> to SARS-CoV-2 interventions. **[SWP: Need to emphasize broader implications.]**

19 Non-pharmaceutical interventions (NPIs) to slow the spread of SARS-CoV-2 disrupted  
 20 the transmission of other human respiratory pathogens, adding uncertainties  
 21 to their future epidemic dynamics and the overall public health burden [1]. As  
 22 NPIs lifted, large heterogeneities in outbreak dynamics were observed across different  
 23 pathogens in different countries, with some pathogens exhibiting earlier resurgences  
 24 than others [2, 3, 4]. Heterogeneities in the overall reduction in transmission and the  
 25 timing of re-emergence likely reflect differences in NPI patterns, pathogen character-  
 26 istics, immigration/importation from other countries, and pre-pandemic pathogen  
 27 dynamics [5]. Therefore, comparing the differential impact of the pandemic pertur-  
 28 bations across pathogens can provide unique opportunities to learn about underlying  
 29 pathogen characteristics, such as their transmissibility or duration of immunity, from  
 30 heterogeneities in re-emergence patterns [6].

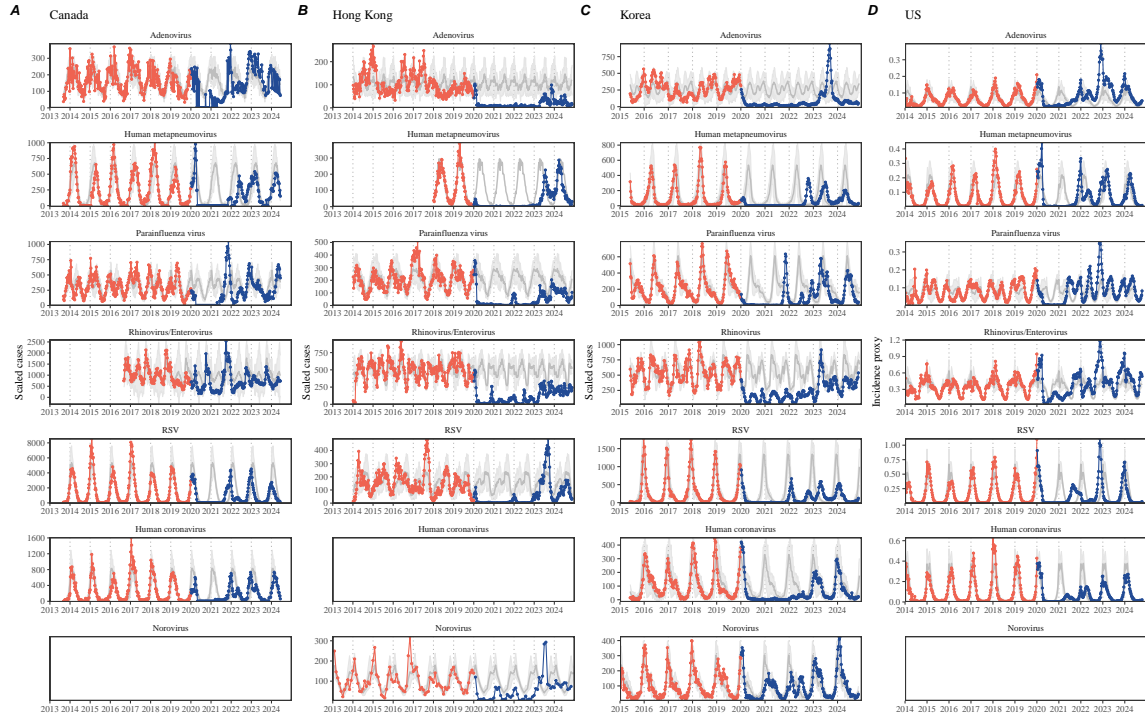


**Figure 1: Observed heterogeneity in responses to pandemic perturbations across respiratory pathogens and norovirus in (A) Canada, (B) Hong Kong, (C) Korea, and (D) US.** Red points and lines represent data before 2020. Blue points and lines represent data since 2020. Gray lines and shaded regions represent the mean seasonal patterns and corresponding 95% confidence intervals around the mean. Mean seasonal patterns were calculated by aggregating cases before 2020 into 52 weekly bins and taking the average in each week. Cases were scaled to account for changes in testing patterns (Materials and Methods).

31 Even though more than five years have passed since the emergence of SARS-CoV-  
 32 2, we still observe persistent changes in pathogen dynamics following the pandemic

33 perturbations: for example, compared to pre-pandemic, seasonal patterns, human  
34 metapneumovirus in Korea seem to circulate at lower levels, whereas RSV in Ko-  
35 rea seem to exhibit different seasonality (Figure 1). These observations suggest a  
36 possibility for a fundamental change in pathogen dynamics following the pandemic  
37 perturbations, which can be driven by permanent shift in either human behavior  
38 or population-level immunity [7, 8]. The possibility of a long-lasting impact of the  
39 pandemic perturbations pose an important question for future infectious disease dy-  
40 namics: can we predict whether and when other respiratory pathogens will eventually  
41 return to their pre-pandemic dynamics? *[SWP: You suggested: I would say some-  
42 thing about the dynamics of these pathogens not being well understood, but I've  
43 since rewritten the most of intro and I'm not sure where I would fit this. If you have  
44 any suggestions, let me know...]*

45 So far, the majority of epidemiological analyses of respiratory pathogens in the  
46 context of the pandemic perturbations have focused on characterizing the timing of  
47 rebound [1, 9, 5]. Instead, we seek to characterize how fast a pathogen returns to its  
48 pre-pandemic dynamics. These two concepts have subtle but important differences:  
49 for example, it took more than 3 years for human metapneumovirus to rebound in  
50 Hong Kong but the observed epidemic patterns in 2024 are similar to pre-pandemic  
51 seasonal means, suggesting a rapid return to pre-pandemic dynamics following a  
52 perturbation (Figure 1). Measuring this rate of return is particularly useful because  
53 it allows us to quantify the ecological resilience of a host-pathogen system [10, 11,  
54 12, 13].

55 In this study, we lay out theoretical and statistical approaches to characterizing  
56 the resilience of a host-pathogen system based on how fast the system recovers from  
57 perturbation. We begin by laying out a few representative scenarios that capture  
58 the potential impact of pandemic perturbations on endemic pathogen dynamics and  
59 illustrate how resilience can be measured by comparing the pre- and post-pandemic  
60 dynamics of susceptible and infected hosts. In practice, information on susceptible  
61 hosts is often unavailable, making this theoretical approach infeasible. Instead, we  
62 utilize a mathematical technique to reconstruct empirical attractors from the data  
63 [14], which allows us to measure the rate at which the host-pathogen system ap-  
64 proaches this empirical attractor after a perturbation; this rate corresponds to the  
65 resilience of the host-pathogen system. We use this method to analyze pathogen  
66 surveillance data for respiratory and non-respiratory pathogens from Canada, Hong  
67 Kong, Korea, and US. Finally, we show that susceptible host dynamics explain vari-  
68 ation in pathogen resilience.

## 69 Conceptual introduction to pathogen resilience

70 In classical ecological literature, resilience of an ecological system is measured by  
71 the rate at which the system returns to its reference state following a perturbation  
72 [10, 11, 12, 13]. This rate corresponds to the largest real part of the eigenvalues of

73 the linearized system near equilibrium—here, we refer to this value as the *intrinsic*  
74 resilience of the system, which represents the expected rate of return from perturbed  
75 states. In practice, we rarely know the true model describing population-level dy-  
76 namics of common respiratory pathogens, limiting our ability to infer the intrinsic  
77 resilience of a system. Instead, we can still measure the *empirical* resilience of a  
78 host-pathogen system by looking at how fast the system returns to the pre-pandemic,  
79 endemic dynamics after interventions are lifted.

80 As an example, we begin with a simple Susceptible-Infected-Recovered-Susceptible  
81 (SIRS) model with seasonally forced transmission and demography (i.e., birth and  
82 death). The SIRS model is the simplest model that allows for waning of immunity  
83 and is commonly used for modeling the dynamics of respiratory pathogens [15]. First,  
84 consider an intervention that reduce transmission by 50% for 6 months starting in  
85 2020, which causes epidemic patterns to deviate from its original stable annual cycle  
86 for a short period of time and eventually come back (Figure 2A). To measure the  
87 resilience of this system empirically, we first need to be able to measure the dis-  
88 tance from its pre-pandemic attractor. There are many ways we can measure the  
89 distance from the attractor, but for illustrative purposes, we choose one of the most  
90 parsimonious approach: that is, we look at how the susceptible (S) and infected (I)  
91 populations change over time and measure the distance on the SI phase plane (Figure  
92 2B). In this simple case, the locally estimated scatterplot smoothing (LOESS) fit in-  
93 dicates that the distance from the attractor decreases exponentially (linearly on a log  
94 scale) on average (Figure 2C). Furthermore, the overall rate of return approximates  
95 the intrinsic resilience of the seasonally unforced system (Figure 2C).

96 Alternatively, pandemic perturbations can have a lasting impact on the pathogen  
97 dynamics; as an example, we consider a scenario in which a 10% reduction in trans-  
98 mission persists even after interevntions are lifted (Figure 2D–F). In such cases in  
99 practice, we cannot know whether the pathogen will return to its original cycle or a  
100 different cycle until many years have passed, and we cannot measure the distance to  
101 the new unknown attractor that the system might eventually approach. Nonethe-  
102 less, we can still measure the distance from the pre-pandemic attractor and ask  
103 how the distance changes over time (Figure 2E). The LOESS fit suggests that the  
104 distance from the pre-pandemic attractor will initially decrease exponentially on av-  
105 erage (equivalently, linearly on a log scale) and eventually plateau (Figure 2F). Here,  
106 a permanent 10% reduction in transmission rate slows the system, which causes the  
107 distance from the pre-pandemic attractor initially to decrease at a slower rate (Figure  
108 2F) than it would have otherwise (Figure 2C) before plateauing at a fixed distance  
109 between the two attractors. This example shows that resilience is not necessarily an  
110 intrinsic property of a specific pathogen. Instead, pathogen resilience is a property  
111 of a specific attractor that a host-pathogen system approaches, which depends on  
112 both pathogen and host characteristics.

113 Finally, transient phenomena can further complicate the picture (Figure 2G–I).  
114 For example, a stage-structured model initially exhibits a stable annual cycle, but  
115 perturbations from a 10% reduction in transmission for 6 months cause the epidemic

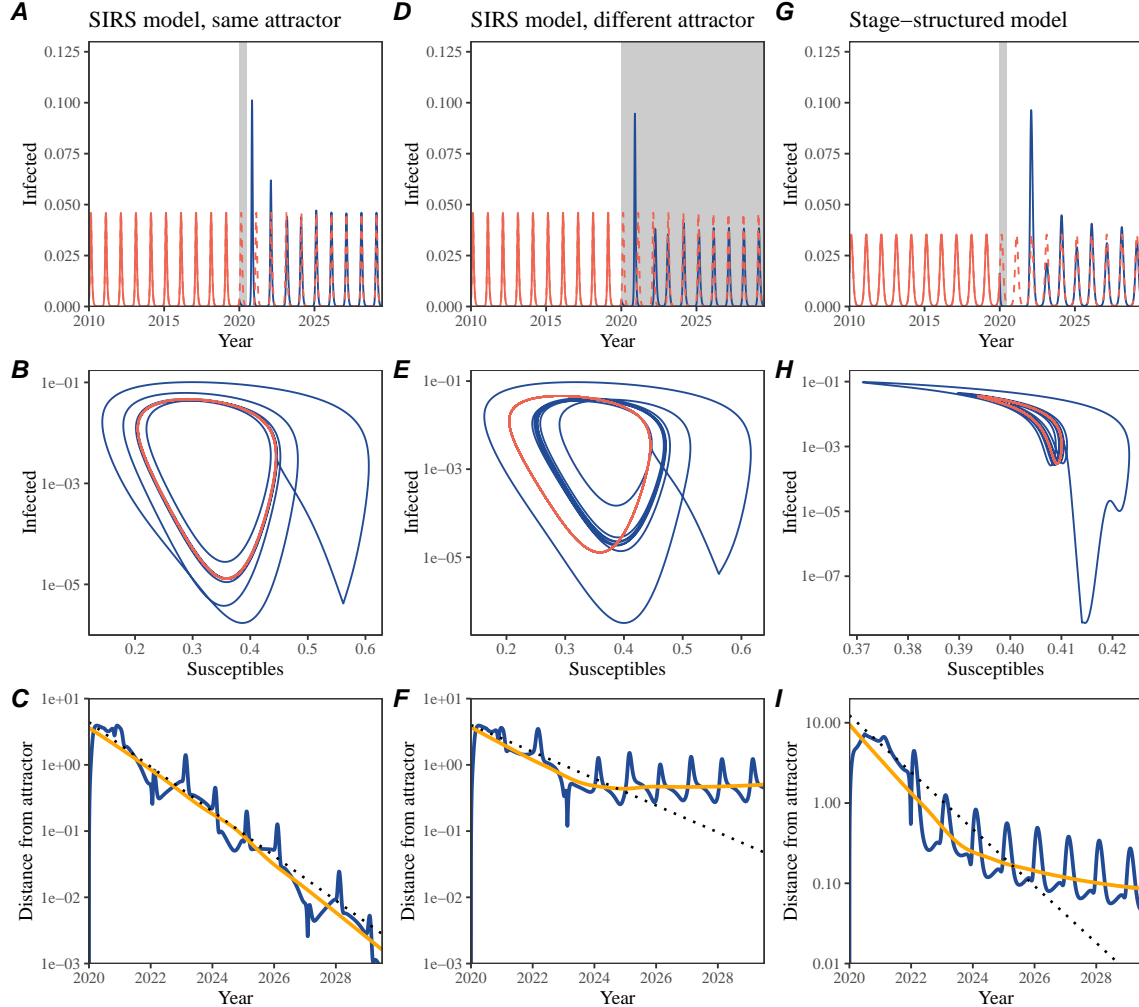


**Figure 2: A simple method to measure pathogen resilience following pandemic perturbations across different scenarios.** (A, D, G) Simulated epidemic trajectories across various models. Red and blue solid lines represent epidemic dynamics before and after interventions are introduced, respectively. Red dashed lines represent counterfactual epidemic dynamics in the absence of interventions. Gray regions indicate the duration of interventions. (B, E, H) Phase plane representation of the time series in panels A, D, and G alongside the corresponding susceptible host dynamics. Red and blue solid lines represent epidemic trajectories on an SI phase plane before and after interventions are introduced, respectively. (C, F, I) Changes in logged distance from the attractor over time. Blue lines represent the logged distance from the attractor. Orange lines represent the locally estimated scatterplot smoothing (LOESS) fits to the logged distance from the attractor. Dotted lines show the intrinsic resilience of the seasonally unforced system.

to shift to biennial cycles (Figure 2G). The system eventually approaches the original

117 pre-pandemic attractor (Figure 2H), suggesting that this biennial cycle is a transient  
118 phenomenon. The LOESS fit indicates that the distance from the attractor initially  
119 decreases exponentially at a rate that is consistent with the intrinsic resilience of  
120 the seasonally unforced stage-structured system, but the rate of decrease decelerates  
121 with the damped oscillations (Figure 2I). This behavior is also referred to as a ghost  
122 attractor, which causes long transient dynamics and slow transitions [16]. Strong  
123 seasonal forcing in transmission can also lead to transient phenomena for a simple  
124 SIRS model, causing a slow return to pre-perturbation dynamics (Supplementary  
125 Figure S1).

126 This empirical approach allows us to measure the resilience of a two-strain host-  
127 pathogen system even when we have incomplete observation of the infection dynam-  
128 ics. Simulations from a simple two-strain system illustrate that separate analyses of  
129 individual strain dynamics (e.g., RSV A vs B) and a joint analysis of total infections  
130 (e.g., total RSV infections) yield identical resilience estimates (Supplementary Fig-  
131 ure S2, 3). This is expected because the dynamics of two strains (or two pathogens)  
132 around the attractor in a coupled system are described by the same set of eigen-  
133 values and eigenvectors, meaning that both strains should exhibit identical rates of  
134 returns following a perturbation. Analogous to a single system, strong seasonal forc-  
135 ing in transmission can cause the system to slow down through transient phenomena  
136 (Supplementary Figure S4).

137 These observations indicate three possibilities. First, we can directly estimate the  
138 empirical resilience of a host-pathogen system by measuring the rate at which the  
139 system approaches an attractor, provided that we have a way to quantify the distance  
140 from the attractor. The empirical approach to estimating pathogen resilience is  
141 particularly convenient because it does not require us to know the true underlying  
142 model; estimating the intrinsic resilience from fitting misspecified models can lead  
143 to biased estimates (Supplementary Figure S5). Second, resilience estimates allow  
144 us to make phenomenological predictions about the dynamics of a host-pathogen  
145 system following a perturbation. Assuming that the distance from the attractor will  
146 decrease exponentially over time, we can obtain a ballpark estimate for when the  
147 system will reach an attractor; this prediction necessarily assumes that there won't  
148 be permanent changes in pathogen dynamics (Figure 2F) or a long-term transient  
149 phenomenon (Figure 2I). Finally, a change in the rate of an exponential decrease in  
150 the distance from the attractor can provide information about whether the system  
151 has reached an alternative attractor, or a ghost attractor, that is different from the  
152 original, pre-pandemic attractor. These alternative attractors may reflect continued  
153 perturbations from permanent changes in transmission patterns as well as changes in  
154 immune landscapes. There will be periods of time when it is difficult to tell whether  
155 pathogen dynamics are still diverging from its original attractor or have begun to  
156 converge to an attractor; now that several years have passed since interventions have  
157 been lifted, we expect many respiratory pathogens to have had sufficient time to  
begin returning to their post-intervention attractors.

159 **Inferring pathogen resilience from real data**

160 Based on these observations, we now lay out our approach to estimating pathogen  
161 resilience from real data (Figure 3). We then test this approach against simulations  
162 and apply it to real data.

163 So far, we focused on simple examples that assume a constant transmission re-  
164 duction. However, in practice, the impact of pandemic perturbations on pathogen  
165 transmission is likely more complex (Figure 3A), reflecting introduction and relax-  
166 ation of various intervention strategies. In some cases, strong perturbations can even  
167 lead to a local fadeout, requiring immigration from another location for epidemic re-  
168 emergence. These complexities can lead to longer delays between the introduction of  
169 pandemic perturbations and pathogen re-emergence as well as temporal variation in  
170 outbreak sizes (Figure 3B): in this example, continued transmission reduction from  
171 interventions limits the size of the first outbreak in 2021 following the emergence,  
172 allowing for a larger outbreak in 2022 when interventions are further relaxed.

173 Previously, we relied on the dynamics of susceptible and infected hosts to com-  
174 pute the distance from the attractor (Figure 2), but information on susceptible hosts  
175 is rarely available in practice. In addition, uncertainties in case counts due to obser-  
176 vation error as well as multiannual cycles in the observed epidemic dynamics (e.g.,  
177 adenovirus circulation patterns in Hong Kong and Korea) add challenges to defin-  
178 ing pre-pandemic attractors, which limits our ability to measure the distance from  
179 the attractor. To address these challenges, we can reconstruct an empirical attrac-  
180 tor by utilizing Takens' theorem [14], which states that an attractor of a nonlinear  
181 multidimensional system can be mapped onto a delayed embedding (Materials and  
182 Methods). For example, we can use delayed logged values of pre-pandemic cases  $C(t)$   
183 (Figure 3C) to reconstruct the attractor:

$$\langle \log(C(t) + 1), \log(C(t - \tau) + 1), \dots, \log(C(t - (M - 1)\tau) + 1) \rangle, \quad (1)$$

184 where the delay  $\tau$  and embedding dimension  $M$  are determined based on autocor-  
185 relations and false nearest neighbors, respectively [17, 18]. We can then apply the  
186 same delay and embedding dimensions to the entire time series to determine the  
187 position on a multi-dimensional state space (Figure 3D), which allows us to mea-  
188 sure the nearest neighbor distance between the current state of the system and the  
189 empirical pre-pandemic attractor (Figure 3E). In theory, we can now quantify how  
190 fast this distance decreases by fitting a linear regression on a log scale, where the  
191 slope of the linear regression corresponds to pathogen resilience. However, resulting  
192 estimates of pathogen resilience can be sensitive to choices about embedding delays  
193 and dimensions; for example, using longer delays and higher dimensions tends to  
194 smooth out temporal variations in the distance from the attractor (Supplementary  
195 Figure S6).

196 Complex changes in the distance from the attractor suggest that estimating  
197 pathogen resilience from linear regression will be particularly sensitive to our choice  
198 of fitting windows for the regression (Figure 3E). Therefore, before we tried estimat-

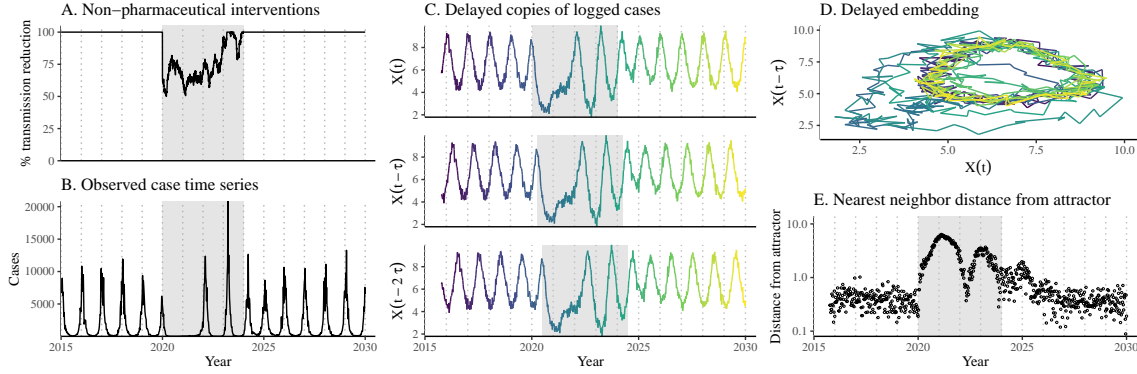


**Figure 3: A schematic diagram explaining the inference of pathogen resilience from synthetic data.** (A) A realistic example of simulated pandemic perturbations, represented by a relative reduction in transmission. (B) The impact of the synthetic pandemic perturbation on epidemic dynamics simulated using a SIRS model with demographic stochasticity. (C) Generating delayed copies of the logged time series allows us to obtain an embedding. (D) Two dimensional representation of an embedding. (E) Delayed embedding allows us to calculate the nearest neighbor distance from the empirical attractor, which is determined based on the pre-pandemic time series. This distance time series can be used to infer pathogen resilience after choosing an appropriate window for linear regression.

199 ing resilience from real data, we explored an automated window selection criterion  
 200 for linear regression and test it against randomized, stochastic simulations across a  
 201 wide range of realistic pandemic perturbation shapes; in doing so, we also explored  
 202 optimal choices for embedding dimensions and evaluated our choices for fitting win-  
 203 dows parameters and embedding dimensions by quantifying correlation coefficients  
 204 between the estimated resilience and the intrinsic resilience of a seasonally unforced  
 205 system (Materials and Methods). Overall, we find large variation in estimation  
 206 performances with correlation coefficient ranging from 0.21 to 0.61 (Supplementary  
 207 Figure S7). In almost all cases, the automated window selection approach outper-  
 208 formed a naive approach that uses the entire time series, starting from the peak  
 209 distance (Supplementary Figure S7).

210 Based on the best performing window selection criteria and embedding dimen-  
 211 sion, we applied this approach to pathogen surveillance data presented in Figure  
 212 1 (Materials and Methods). For each time series, we applied Takens' theorem in-  
 213 dependently to reconstruct the empirical attractor and obtained the corresponding  
 214 time series of distances from attractors (Supplementary Figure S8). Then, we use  
 215 the automated window selection criterion to fit a linear regression and estimate the  
 216 empirical resilience for each pathogen in each country (Supplementary Figure S8);  
 217 the window selection criterion gave poor regression window for three cases (norovirus  
 218 in Hong Kong and Korea and Rhinovirus/Enterovirus in the US), leading to unreal-  
 219 istically low resilience estimates, and so we used ad-hoc regression windows instead

220 (Supplementary Figure S9; Materials and Methods).

221 For all pathogens we consider, resilience estimates fall between 0.4/year and  
222 1.8/year (Figure 4A). We estimate the mean resilience of common respiratory pathogens  
223 to be 0.99/year (95% CI: 0.80/year–1.18/year). As a reference, this is  $\approx$  7.5 times  
224 higher than the intrinsic resilience of pre-vaccination measles in England and Wales  
225 ( $\approx$  0.13/year). Finally, resilience estimates for norovirus are comparable to those of  
226 common respiratory pathogens: 1.44/year (95%CI: 1.01/year–1.87/year) for Hong  
227 Kong and 1.07/year (95%CI: 0.86/year–1.29/year) for Korea. Based on a simple  
228 ANOVA test, we do not find significant differences in resilience estimates across  
229 countries ( $p = 0.25$ ) or pathogens ( $p = 0.68$ ).

230 [SWP: You suggested “I think we probably need to spell out a bit more that  
231 long-term changes in the transmission rate (or some other parameter) mean the at-  
232 tractor is permanently different and the distance should remain nonzero” and I think  
233 we’ve done that enough early on with current revisions so I don’t feel like we need  
234 to do it again here. Let me know what you think.] Using resilience estimates, we  
235 predicted when each pathogen would hypothetically return to their pre-pandemic  
236 dynamics, assuming no long-term change in the attractor. Specifically, we extend  
237 our linear regression fits to distance-from-attractor time series and ask when the pre-  
238 dicted regression line will cross a threshold value; since we relied on nearest neighbor  
239 distances, pre-pandemic distances are always greater than zero (Figure 3E), meaning  
240 that we can use the mean of pre-pandemic distances as our threshold.

241 We predict that a return to pre-pandemic cycles would be imminent for most  
242 pathogens (Figure 4B). In particular, we predict that 12 out of 23 pathogens should  
243 have already returned before the end of 2024. For almost all pathogens that are  
244 predicted to have returned already, the observed epidemic dynamics show clear con-  
245 vergence towards their pre-pandemic seasonal averages, confirming our predictions  
246 (Figure 4C). However, there are a few exceptions, including norovirus in Hong Kong  
247 and Rhinovirus/Enterovirus in the US, where the observed epidemic dynamics in  
248 2024 exhibit clear deviation from their pre-pandemic seasonal averages (Figure 4C).  
249 These observations suggest a possibility that some common respiratory pathogens  
250 may have converged to different attractors or are still exhibiting non-equilibrium  
251 dynamics. In contrast, pathogens that are predicted to have not returned yet also  
252 show clear differences from their pre-pandemic seasonal averages; as many of these  
253 pathogens are predicted to return in 2025–2026, we may be able to test these pre-  
254 dictions in near future (Supplementary Figure S10). Our reconstructions of distance  
255 time series and estimates of pathogen resilience and expected return time are gener-  
256 ally robust to choices of embedding dimensions (Supplementary Figure S11–12).

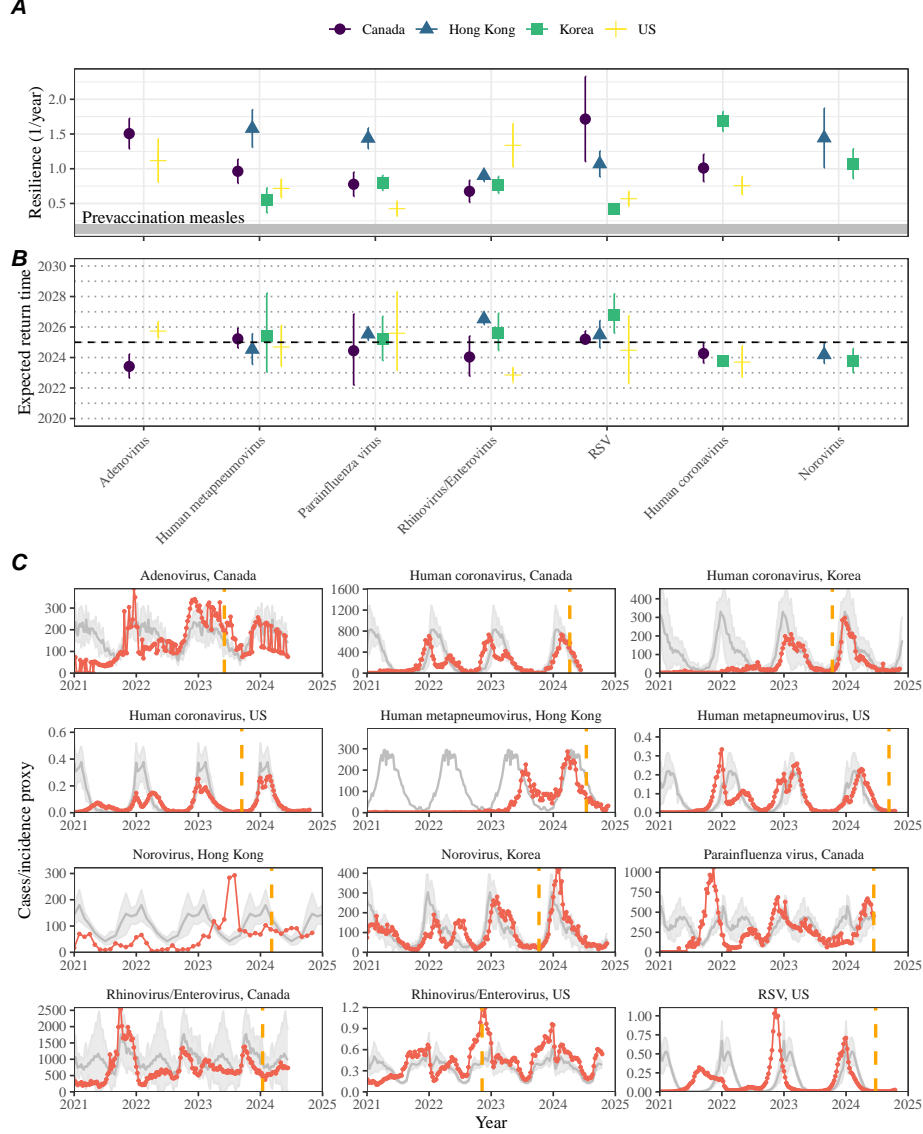


**Figure 4: Summary of resilience estimates and predictions for return time.** (A) Estimated pathogen resilience. The gray horizontal line represents the intrinsic resilience of pre-vaccination measles dynamics. (B) Predicted timing of when each pathogen will return to their pre-pandemic cycles. The dashed line in panel B indicates the end of 2024 (current observation time). Error bars represent 95% confidence intervals. (C) Observed dynamics for pathogen that are predicted to have returned before the end of 2024. Red points and lines represent data before 2020. Gray lines and shaded regions represent the mean seasonal patterns and corresponding 95% confidence intervals around the mean, previously shown in Figure 1. Orange vertical lines represent the predicted timing of return.

257 **Susceptible host dynamics explain variation in pathogen  
258 resilience**

259 So far, we focused on quantifying pathogen resilience from the observed patterns  
260 of pathogen re-emergence following pandemic perturbations. But what factors de-  
261 termine how resilient a host-pathogen system is? Here, we use the SIRS model to  
262 show that susceptible host dynamics are the key determinants of pathogen resilience.  
263 To do so, we vary the basic reproduction number  $\mathcal{R}_0$ , which represents the average  
264 number of secondary infections caused by a newly infected individual in a fully sus-  
265 ceptible population, and the duration of immunity and compute intrinsic resilience  
266 for each parameter.

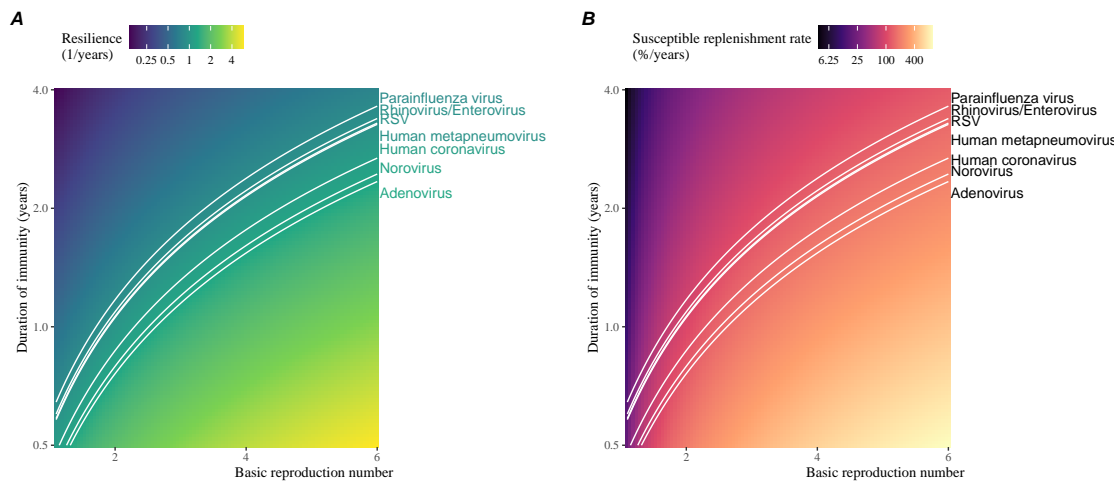


Figure 5: **Linking pathogen resilience to epidemiological parameters and susceptible host dynamics.** (A) The heat map represents intrinsic resilience as a function of the basic reproduction number  $\mathcal{R}_0$  and the duration of immunity. (B) The heat map represents per-capita susceptible replenishment rate as a function of the basic reproduction number  $\mathcal{R}_0$  and the duration of immunity. The standard SIRS model is used to compute intrinsic resilience and per-capita susceptible replenishment rate. Lines correspond to a set of parameters that are consistent with mean resilience estimates for each pathogen. Pathogens are ranked based on their mean resilience estimates, averaged across different countries.

267 We find an increase in  $\mathcal{R}_0$  and a decrease in duration of immunity correspond  
268 to an increase in pathogen resilience (Figure 5A). These variations can be under-  
269 stood in terms of the susceptible host dynamics, where faster per-capita susceptible  
270 replenishment rate causes the system to be more resilient (Figure 5B). This rate can  
271 be expressed as a ratio between absolute rate at which new susceptibles enter the  
272 population and the equilibrium number of susceptible individuals in the population,  
273  $\bar{S}$ . Therefore, both higher  $\mathcal{R}_0$  and shorter duration of immunity can drive faster

274 per-capita susceptible replenishment rate (Figure 5B), especially because higher  $\mathcal{R}_0$   
275 leads to lower  $\bar{S}$ .

276 We can also rank different pathogens based on the average values of empirical  
277 resilience computed previously, which allows us to determine a set of parameters that  
278 are consistent with the estimated resilience (Figure 5A). Across all pathogens we  
279 consider, except for bocavirus and norovirus, we estimate that the average duration  
280 of immunity is likely to be short (< 4 years) across a plausible range of  $\mathcal{R}_0$  (< 6).  
281 These rankings further allow us to map each pathogen onto a set of SIRS parameters  
282 that are consistent with its empirical resilience (Figure 5A) and obtain a plausible  
283 range of susceptible replenishment rates for each pathogen (Figure 5B). However, we  
284 note that there is no one-to-one correspondence between susceptible replenishment  
285 rates and pathogen resilience, leading to a wide uncertainty in the estimates for  
286 susceptible replenishment rates (Figure 5B).

## 287 **Pathogen resilience determines sensitivity to stochastic perturbations**

288

289 Beyond the pandemic perturbations, we expect host-pathogen systems to experience  
290 continued perturbations of varying degrees from changes in epidemiological conditions,  
291 such as human behavior, climate, and viral evolution. These perturbations  
292 can also arise from demographic stochasticity, which is inherent to any ecological  
293 systems. Here, we use a seasonally unforced SIRS model with birth/death to explore  
294 how resilience of a host-pathogen system determines the sensitivity to perturbations  
295 caused by demographic stochasticity (Materials and Methods).

296 We find that resilience of a host-pathogen system determines the amount of deviation  
297 from the deterministic trajectory caused by demographic stochasticity, with less  
298 resilient systems experiencing larger deviations (Figure 6). Notably, less resilience  
299 systems also exhibit slower epidemic cycles; the periodicity of this epidemic cycle  
300 matches those predicted by the intrinsic periodicity of the system (Supplementary  
301 Figure S13). These conclusions are robust for the seasonally forced SIRS model  
302 (Supplementary Figure S14),

## 303 **Discussion**

304 The pandemic interventions have caused major disruptions to circulation patterns of  
305 both respiratory and non-respiratory pathogens, adding challenges to predicting their  
306 future dynamics [1, 2, 3, 4]. However, these perturbations offer large-scale natural  
307 experiments for understanding how different pathogens respond to perturbations. In  
308 this study, we showed that pathogen re-emergence patterns following pandemic per-  
309 turbations can be characterized through the lens of ecological resilience. We showed  
310 that variation in pathogen resilience can be explained by the differences in suscepti-

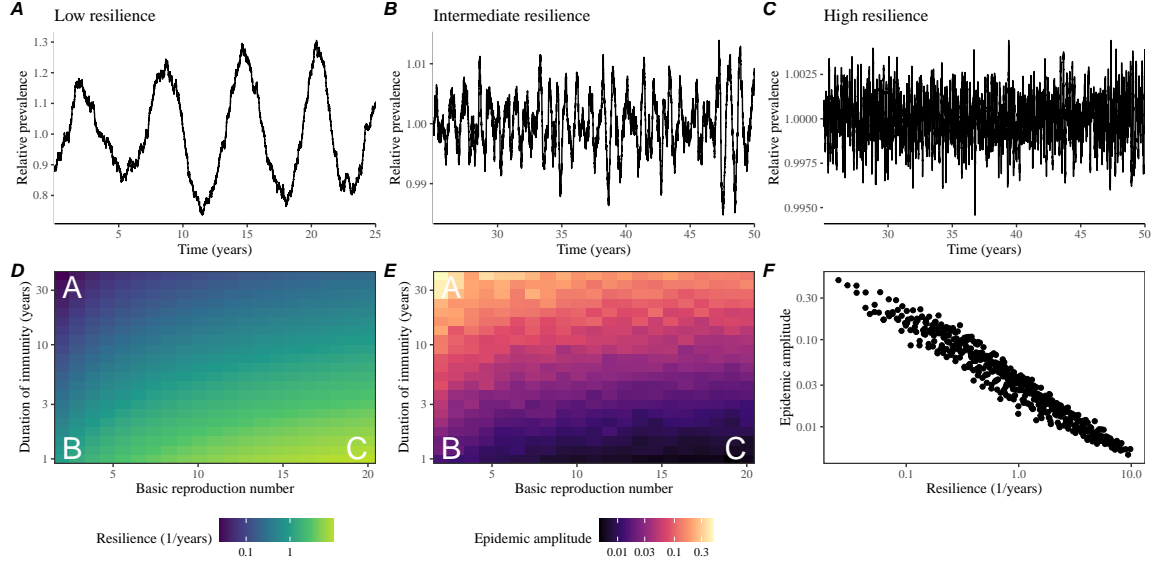


**Figure 6: Linking resilience of a host-pathogen system to its sensitivity to stochastic perturbations.** (A–C) Epidemic trajectories of a stochastic SIRS model across three different resilience values: low, intermediate, and high. The relative prevalence was calculated by dividing infection prevalence by its mean value. (D) The heat map represents the intrinsic resilience of a system as a function of the basic reproduction number  $\mathcal{R}_0$  and the duration of immunity. (E) The heat map represents the epidemic amplitude as a function of the basic reproduction number  $\mathcal{R}_0$  and the duration of immunity. The epidemic amplitude corresponds to  $(\max I - \min I)/(2\bar{I})$ , where  $\bar{I}$  represents the mean prevalence. (F) The relationship between pathogen resilience and epidemic amplitude.

311   ble host dynamics, where faster replenishment of the susceptible pool corresponds to  
 312   a more resilient host-pathogen system. Finally, we showed that pathogen resilience  
 313   also determines the sensitivity to stochastic perturbations.

314   We analyzed case time series of common respiratory infections and norovirus  
 315   infections from Canada, Hong Kong, Korea, and the US to estimate their resilience.  
 316   Overall, we estimated the resilience of these pathogens to range from 0.4/year to  
 317   1.8/year, which is 3–14 times more resilient than prevaccination measles. These  
 318   resilience estimates indicate that common respiratory pathogens and norovirus likely  
 319   exhibit faster susceptible replenishment and are therefore more persistent, indicating  
 320   potential challenges in controlling these pathogens.

321   Based on our resilience estimates, we made phenomenological predictions about  
 322   when each pathogen will return to their endemic cycles. For the most part, we  
 323   accurately predicted which pathogens should have already returned before the end  
 324   of 2024. However, there were few exceptions (i.e., norovirus in Hong Kong and  
 325   rhinovirus/enterovirus in the US), suggesting a possibility that these may have con-

326 verged to different endemic cycles compared to their pre-pandemic epidemic patterns.  
327 These changes may reflect changes in surveillance or actual shift in the dynamics,  
328 caused by permanent changes in behavior or population-level immunity. While it may  
329 seem unlikely that permanent changes in behavior would only affect a few pathogens  
330 and not others, we cannot rule out this possibility given heterogeneity in the age of  
331 infection across different respiratory pathogens [19, 20]. Differences in the mode of  
332 transmission between respiratory vs gastrointestinal pathogens may also contribute  
333 to the differences in responses to pandemic perturbations. However, it is unclear  
334 why norovirus dynamics in Korea seemed to have returned, whereas those in Hong  
335 Kong have not.

336 For almost half of the pathogens we considered, we predicted that their return  
337 to original epidemic patterns is imminent. We will need a few more years of data  
338 to test whether these pathogens will eventually return to their original dynamics  
339 or eventually converge to a different attractor. Overall, these observations echo  
340 earlier studies that highlighted the long-lasting impact of pandemic perturbations  
341 [8, 21, 22, 4].

342 We showed that susceptible host dynamics shape pathogen resilience, where faster  
343 replenishment of the susceptible population causes the pathogen to be more resilient.  
344 For simplicity, we focus on waning immunity and birth as the main drivers of the  
345 susceptible host dynamics but other mechanisms can also contribute to the replen-  
346 ishment of the susceptible population. In particular, pathogen evolution, especially  
347 the emergence of antigenically novel strains, can cause effective waning of immunity  
348 in the population; therefore, we hypothesize that faster rates of antigenic evolution  
349 can also cause a pathogen to be more resilient. Future studies should explore the  
350 relationship between the rate of evolution and resilience for antigenically evolving  
351 pathogens.

352 Quantifying pathogen resilience also offers novel approaches to validating population-  
353 level epidemiological models. So far, most of model validation in infectious disease  
354 ecology is based on the ability of a model to reproduce the observed epidemic dy-  
355 namics and to predict future dynamics [23, 24, 25, 26, 27]. However, many models  
356 can perform similarly under these criteria. For example, two major RSV models  
357 have been proposed to explain biennial epidemic patterns: (1) a stage- and age-  
358 structured model that allows disease severity to vary with number of past infections  
359 and age of infection [25] and (2) a pathogen-interaction model that accounts for cross  
360 immunity between RSV and human metapneumovirus [24]. Since both models can  
361 accurately reproduce the observed epidemic patterns, standard criteria for model  
362 validation do not allow us to distinguish between these two models from population-  
363 level data alone. Instead, it would be possible to measure the empirical resilience of  
364 each model by simulating various perturbations and compare them to estimates of  
365 empirical resilience from data, using pandemic NPIs as an opportunity.

366 There are several limitations to our work. First, we did not extensively explore  
367 other approaches to reconstructing the attractor. Recent studies showed that more  
368 sophisticated approaches, such as using non-uniform embedding, can provide more

robust reconstruction for noisy data [18]. In the context of causal inference, choices about embedding can have major impact on the resulting inference [28]. Our resilience estimates are likely overly confident given a lack of uncertainties in attractor reconstruction as well as the simplicity of our statistical framework. Nonetheless, as illustrated in our sensitivity analyses, inferences about pathogen resilience in our SIRS model appear to be robust to decisions about embedding lags and dimensions—this is because tracking the rate at which the system approaches the attractor is likely a much simpler problem than making inferences about causal directionality. Short pre-pandemic time series also limit our ability to accurately reconstruct the attractor and contribute to the crudeness of our resilience estimates; although this is less likely a problem for respiratory pathogens that are strongly annual, our attractor reconstruction may be inaccurate for those exhibiting multi-annual cycles, such as adenovirus in Hong Kong and Korea. Despite these limitations, our qualitative prediction that common respiratory pathogens are more resilient than prevaccination measles is also likely to be robust, given how rapid many respiratory pathogens returned to their original cycles following pandemic NPIs.

Predicting the impact of anthropogenic changes on infectious disease dynamics is a fundamental aim of infectious disease research in a rapidly changing world. Our study illustrates that quantifying pathogen resilience can help us understand how infectious disease pathogens respond to major perturbations caused by NPIs. More broadly, a detailed understanding of the determinants of pathogen resilience may offer unique insights into pathogen persistence and controllability.

## Materials and Methods

### Data

We gathered time series on respiratory infections from Canada, Hong Kong, Korea, and United States (US). As a reference, we also included time series data on norovirus infections for available countries. In contrast to respiratory pathogens, we expect gastrointestinal viruses, such as norovirus, to be differently affected by pandemic perturbations.

Weekly time series of respiratory infection cases in Canada comes from a publicly available website by the Respiratory Virus Detection Surveillance System, which collect data from select laboratories across Canada [29]. Weekly time series of respiratory infection cases in Hong Kong comes from a publicly available website by the Centre for Health Protection, Department of Health [30]. Weekly time series of acute respiratory infection cases in Korea comes from a publicly available website by the Korea Disease Control and Prevention Agency [31]. Finally, weekly time series of respiratory infection cases in the US were obtained from the National Respiratory and Enteric Virus Surveillance System.

407 **Data processing**

408 For all time series, we rounded every year to 52 weeks by taking the average number  
409 of cases and tests between the 52nd and 53rd week. We also rescale all time series to  
410 account for changes in testing patterns, which are then used for the actual analysis.

411 Canada: To account for an increase in testing from 2013 to 2024, we calculate  
412 a 2 year moving average for the number of tests for each pathogen, which we use  
413 as a proxy for testing effort. Then, we divide the smoothed testing patterns by the  
414 smoothed value at the final week such that the testing effort has a maximum of 1.  
415 We then divide weekly cases by the testing effort to obtain a scaled case time series.  
416 A similar approach was used earlier for the analysis of RSV time series in the US  
417 [25].

418 Hong Kong: We also apply the same scaling procedure to the time series as we did  
419 for Canada. For Hong Kong, we only adjust for testing efforts up to the end of 2019  
420 because there was a major reduction in testing for common respiratory pathogens  
421 since 2020.

422 Korea: While we do not have information on testing, the reported number of  
423 respiratory infections consistently increased from 2013 to the end of 2019, which we  
424 interpreted as changes in testing patterns. Since we do not have testing numbers,  
425 we used the weekly sum of all acute respiratory viral infection cases as a proxy for  
426 testing, which were further smoothed with moving averaged and scaled to have a  
427 maximum of 1. For Korea, we also only adjust for testing efforts up to the end of  
428 2019.

429 US: In the US, there has been a large increase in testing against some respira-  
430 tory pathogens, especially RSV, which could not be corrected for through simple  
431 scaling. Instead, we derive an incidence proxy by multiplying the test positivity  
432 with influenza-like illness positivity, which is taken from [https://gis.cdc.gov/  
433 grasp/fluview/fluportaldashboard.html](https://gis.cdc.gov/grasp/fluview/fluportaldashboard.html). This method of estimating an inci-  
434 dence proxy has been recently applied in the analysis of seasonal coronaviruses [7]  
435 and *Mycoplasma pneumoniae* infections [4]. Detailed assumptions and justifications  
436 are provided in [32].

437 **Estimating pathogen resilience**

438 In order to measure pathogen resilience from surveillance data, we first reconstruct  
439 the empirical pre-pandemic attractor of the system using Takens' embedding theorem  
440 [14]. Specifically, for a given pathogen, we take the pre-pandemic (before 2020)  
441 case time series  $C(t)$  and reconstruct the attractor using delayed embedding with a  
442 uniform delay of  $\tau$  and dimension  $M$ :

$$X_{\tau,m}(t) = \langle \log(C(t) + 1), \log(C(t - \tau) + 1), \dots, \log(C(t - (M - 1)\tau) + 1) \rangle. \quad (2)$$

443 Here, the delay  $\tau$  is determined by calculating the autocorrelation of the logged pre-  
444 pandemic time series and asking when the autocorrelation crosses 0 for the first time  
445 [18]; a typical delay for an annual outbreak is around 13 weeks.

446 Then, for a given delay  $\tau$ , we determine the embedding dimension  $M$  using the  
 447 false nearest neighbors approach [17, 18]. To do so, we start with an embedding  
 448 dimension  $e$  and construct a set of points  $A_{\tau,e} = \{X_{\tau,e}(t) | t < 2020\}$ . Then, for  
 449 each point  $X_{\tau,e}(t)$ , we determine the nearest neighbor from the set  $A_{\tau,e}$ , which we  
 450 denote  $X_{\tau,e}(t_{nn})$  for  $t \neq t_{nn}$ . Then, if the distance between these two points on  
 451  $e + 1$  dimension,  $D_{\tau,e+1}(t) = \|X_{\tau,e+1}(t_{nn}) - X_{\tau,e+1}(t)\|_2$ , is larger than their distance  
 452 on  $e$  dimension,  $D_{\tau,e}(t) = \|X_{\tau,e}(t_{nn}) - X_{\tau,e}(t)\|_2$ , these two points are deemed to  
 453 be false nearest neighbors; specifically, we use a threshold  $R$  for the ratio between  
 454 two distances  $D_{\tau,e+1}(t)/D_{\tau,e}(t)$  to determine false nearest neighbors. In the main  
 455 text, we determine the embedding dimension based on the first dimension without  
 456 any false nearest neighbors for  $R = 10$ . In Supplementary Materials, we impose  
 457  $R = 5$  to select for higher dimensions. Once we determine the embedding lag  $\tau$   
 458 and dimension  $M$ , we apply the embedding to the entire time series and calculate  
 459 the nearest neighbor distance against the attractor  $A_{\tau,M}$  to obtain a time series of  
 460 distance from the attractor  $D_{\tau,M}(t)$ .

461 From a time series of distances from the attractor, we estimate pathogen resilience  
 462 by fitting a linear regression to an appropriate window. To automatically select  
 463 the fitting window, we begin by smoothing the distance time series using locally  
 464 estimated scatterplot smoothing (LOESS) to obtain  $\hat{D}_{\tau,M}(t)$ , where the smoothing  
 465 is performed on a log scale and exponentiated afterwards. Then, we determine  
 466 threshold values ( $T_{\text{start}}$  and  $T_{\text{end}}$ ) for the smoothed distances and choose the fitting  
 467 window based on when  $\hat{D}_{\tau,M}(t)$  crosses these threshold values for the first time.  
 468 These thresholds are determined by first calculating maximum distance,

$$\max \hat{D} = \max \hat{D}_{\tau,M}(t), \quad (3)$$

469 and mean pre-pandemic distance,

$$\hat{D}_{\text{mean}} = \frac{1}{N_{t<2020}} \sum_{t<2020} \hat{D}_{\tau,M}(t), \quad (4)$$

470 as a reference, and then dividing their ratios into 10 equal bins:

$$T_{\text{start}} = \hat{D}_{\text{mean}} \times \left( \frac{\max \hat{D}}{\hat{D}_{\text{mean}}} \right)^{9/10} \quad (5)$$

$$T_{\text{end}} = \hat{D}_{\text{mean}} \times \left( \frac{\max \hat{D}}{\hat{D}_{\text{mean}}} \right)^{1/10} \quad (6)$$

471 This allows us to discard the initial period during which the distance increases (from  
 472 the introduction of intervention measures) and the final period during which the  
 473 distance plateaus (as the system reaches an attractor). The fitting window is deter-  
 474 mined based on when the smoothed distance  $\hat{D}_{\tau,M}(t)$  crosses these threshold values  
 475 for the first time; then, we fit a linear regression to logged (unsmoothed) distances  
 476  $\log D_{\tau,M}(t)$  using that window.

477 **Mathematical modeling**

478 Throughout the paper, we use a series of mathematical models to illustrate the con-  
 479 cept of pathogen resilience and to understand the determinants of pathogen resilience.  
 480 In general, the intrinsic resilience for a given system is given by the largest real part  
 481 of the eigenvalues of the linearized system at endemic equilibrium. Here, we focus on  
 482 the SIRS model with demography and present the details of other models in Supple-  
 483 mentary Materials. The SIRS (Susceptible-Infected-Recovered-Susceptible) model is  
 484 the simplest model that allows for waning of immunity, where recovered (immune)  
 485 individuals are assumed to become fully susceptible after an average of  $1/\delta$  time pe-  
 486 riod. The dynamics of the SIRS model is described by the following set of differential  
 487 equations:

$$\frac{dS}{dt} = \mu - \beta(t)SI - \mu S + \delta R \quad (7)$$

$$\frac{dI}{dt} = \beta(t)SI - (\gamma + \mu)I \quad (8)$$

$$\frac{dR}{dt} = \gamma I - (\delta + \mu)R \quad (9)$$

$$(10)$$

488 where  $\mu$  represents the birth/death rate,  $\beta(t)$  represents the time-varying trans-  
 489 mission rate, and  $\gamma$  represents the recovery rate. The basic reproduction number  
 490  $\mathcal{R}_0(t) = \beta(t)/(\gamma + \mu)$  is defined as the average number of secondary infections that  
 491 a single infected individual would cause in a fully susceptible population at time  $t$   
 492 and measures the intrinsic transmissibility of a pathogen.

493 When we first introduce the idea of pathogen resilience (Figure 2), we impose  
 494 sinusoidal changes to the transmission rate to account for seasonal transmission:

$$\beta(t) = b_1(1 + \theta \cos(2\pi(t - \phi)))\alpha(t), \quad (11)$$

495 where  $b_1$  represents the baseline transmission rate,  $\theta$  represents the seasonal am-  
 496 plitude, and  $\phi$  represents the seasonal offset term. Here, we also introduce an ex-  
 497 tra multiplicative term  $\alpha(t)$  to account for the impact of pandemic NPIs, where  
 498  $\alpha(t) < 1$  indicates transmission reduction. Figure 2A and 2B are generated assum-  
 499 ing  $b_1 = 3 \times (365/7 + 1/50)/\text{years}$ ,  $\theta = 0.2$ ,  $\phi = 0$ ,  $\mu = 1/50/\text{years}$ ,  $\gamma = 365/7/\text{years}$ ,  
 500 and  $\delta = 1/2/\text{years}$ . In Figure 2A, we impose a 50% transmission reduction for 6  
 501 months from 2020:

$$\alpha(t) = \begin{cases} 0.5 & 2020 \leq t < 2020.5 \\ 1 & \text{otherwise} \end{cases} \quad (12)$$

502 In Figure 2B, we impose a 50% transmission reduction for 6 months from 2020 and  
 503 a permanent 10% reduction onward:

$$\alpha(t) = \begin{cases} 1 & t < 2020 \\ 0.5 & 2020 \leq t < 2020.5 \\ 0.9 & 2020.5 \leq t \end{cases} \quad (13)$$

504 In both scenarios, we simulate the SIRS model from the following initial conditions  
 505 ( $S(0) = 1/\mathcal{R}_0$ ,  $I(0) = 1 \times 10^{-6}$ , and  $R(0) = 1 - S(0) - I(0)$ ) from 1900 until 2030.

506 To measure the empirical resilience of the SIR model (Figure 2C and 2F), we  
 507 compute the normalized distance between post-intervention susceptible and logged  
 508 infected proportions and their corresponding pre-intervention values at the same time  
 509 of year:

$$\sqrt{\left(\frac{S(t) - S_{\text{pre}}(t)}{\sigma_S}\right)^2 + \left(\frac{\log I(t) - \log I_{\text{pre}}(t)}{\sigma_{\log I}}\right)^2}, \quad (14)$$

510 where  $\sigma_S$  and  $\sigma_{\log I}$  represent the standard deviation in the pre-intervention suscep-  
 511 tible and logged infected proportions. We normalize the differences in susceptible  
 512 and logged infected proportions to allow both quantities to equally contribute to the  
 513 changes in distance from the attractor. We used logged prevalence, instead of abso-  
 514 lute prevalence, in order to capture epidemic dynamics in deep troughs during the  
 515 intervention period. In Supplementary Materials, we also compare how the degree  
 516 of seasonal transmission affects empirical resilience by varying  $\theta$  from 0 to 0.4; when  
 517 we assume no seasonality ( $\theta = 0$ ), we do not normalize the distance because the  
 518 standard deviation of pre-intervention dynamics are zero.

519 Finally, we use the SIRS model to understand how underlying epidemiological  
 520 parameters affect pathogen resilience and link this relationship to underlying sus-  
 521 ceptible host dynamics. For the simple SIRS model without seasonal transmission  
 522 ( $\theta = 0$ ), the intrinsic resilience corresponds to

$$-\frac{\text{Re}(\lambda)}{2} = \frac{\delta + \beta I^* + \mu}{2}. \quad (15)$$

523 Here,  $I^*$  represents the prevalence at endemic equilibrium:

$$I^* = \frac{(\delta + \mu)(\beta - (\gamma + \mu))}{\beta(\delta + \gamma + \mu)}. \quad (16)$$

524 The susceptible replenishment rate is given by

$$S_{\text{replenish}} = \frac{\mu + \delta R}{S^*}, \quad (17)$$

525 where  $S^* = 1/\mathcal{R}_0$  represents the equilibrium proportion of susceptible individuals.  
 526 We vary the basic reproduction number  $\mathcal{R}_0$  between 1.1 to 6 and the average duration  
 527 of immunity  $1/\delta$  between 2 to 80 years, and compute these two quantities. In doing  
 528 so, we fix all other parameters:  $\mu = 1/80/\text{years}$  and  $\gamma = 365/7/\text{years}$ .

## 529 Data availability

## 530 Funding

531 **Supplementary Text**

532 **Resilience of a stage-structured system.**

533 In Figure 2G–I, we use a more realistic, stage-structured model to illustrate how  
 534 transient phenomena can cause the system to slow down. Specifically, we use the  
 535 stage-structured RSV model proposed by [25], which assumes that subsequent rein-  
 536 fections cause an individual to become less susceptible and transmissible than previ-  
 537 ous infections. The model dynamics can be described as follows:

$$\frac{dM}{dt} = \mu - (\omega + \mu)M \quad (S1)$$

$$\frac{dS_0}{dt} = \omega M - (\lambda(t) + \mu)S_0 \quad (S2)$$

$$\frac{dI_1}{dt} = \lambda(t)S_0 - (\gamma_1 + \mu)I_1 \quad (S3)$$

$$\frac{dS_1}{dt} = \gamma_1 I_1 - (\sigma_1 \lambda(t) + \mu)S_1 \quad (S4)$$

$$\frac{dI_2}{dt} = \sigma_1 \lambda(t)S_1 - (\gamma_2 + \mu)I_2 \quad (S5)$$

$$\frac{dS_2}{dt} = \gamma_2 I_2 - (\sigma_2 \lambda(t) + \mu)S_2 \quad (S6)$$

$$\frac{dI_3}{dt} = \sigma_2 \lambda(t)S_2 - (\gamma_3 + \mu)I_3 \quad (S7)$$

$$\frac{dS_3}{dt} = \gamma_3 I_3 - (\sigma_3 \lambda(t) + \mu)S_3 + \gamma_4 I_4 \quad (S8)$$

$$\frac{dI_4}{dt} = \sigma_3 \lambda(t)S_3 - (\gamma_4 + \mu)I_4 \quad (S9)$$

(S10)

538 where  $M$  represents the proportion of individuals who are maternally immune;  $S_i$   
 539 represents the proportion of individuals who are susceptible after  $i$  prior infections;  $I_i$   
 540 represents the proportion of individuals who are currently (re)-infected with their  $i$ -th  
 541 infection;  $\mu$  represents the birth and death rates;  $1/\omega$  represents the mean duration  
 542 of maternal immunity;  $1/\gamma_i$  represents the mean duration of infection;  $\lambda(t)$  represents  
 543 the force of infection; and  $\sigma_i$  represents the reduction in susceptibility for the  $i$ -th  
 544 reinfection. The force of infection is modeled using a sinusoidal function:

$$\beta(t) = b_1(1 + \theta \cos(2\pi(t - \phi)))\alpha(t) \quad (S11)$$

$$\lambda(t) = \beta(I_1 + \rho_1 I_2 + \rho_2(I_3 + I_4)), \quad (S12)$$

545 where  $b_1$  represents the baseline transmission rate;  $\theta$  represents the seasonal ampli-  
 546 tude;  $\phi$  represents the seasonal offset term;  $\alpha(t)$  represents the intervention effect;  
 547 and  $\rho_i$  represents the impact of immunity on transmission reduction. We use the

548 following parameters to simulate the impact of interventions on epidemic dynam-  
 549 ics [25]:  $b_1 = 9 \times (365/10 + 1/80)/\text{years}$ ,  $\theta = 0.2$ ,  $\phi = -0.1$ ,  $\omega = 365/112/\text{years}$ ,  
 550  $\gamma_1 = 365/10/\text{years}$ ,  $\gamma_2 = 365/7/\text{years}$ ,  $\gamma_3 = 365/5/\text{years}$ ,  $\sigma_1 = 0.76$ ,  $\sigma_2 = 0.6$ ,  
 551  $\sigma_3 = 0.4$ ,  $\rho_1 = 0.75$ ,  $\rho_2 = 0.51$ , and  $\mu = 1/80/\text{years}$ . We assume a 50% transmission  
 552 reduction for 6 months from 2020:

$$\alpha(t) = \begin{cases} 0.5 & 2020 \leq t < 2020.5 \\ 1 & \text{otherwise} \end{cases} \quad (\text{S13})$$

553 The model is simulated from 1900 to 2030 using the following initial conditions:  
 554  $M = 0$ ,  $S_0 = 1/\mathcal{R}_0 - I_1$ ,  $I_1 = 1 \times 10^{-6}$ ,  $S_1 = 1 - 1/\mathcal{R}_0$ ,  $I_2 = 0$ ,  $S_2 = 0$ ,  $I_3 = 0$ ,  
 555  $S_3 = 0$ , and  $I_4 = 0$ . For the phase plane analysis (Figure 2H) and distance analysis  
 556 (Figure 2I), we rely on the average susceptibility,

$$\bar{S} = S_0 + \sigma_1 S_1 + \sigma_2 S_2 + \sigma_3 S_3, \quad (\text{S14})$$

557 and total prevalence,

$$I_{\text{total}} = I_1 + I_2 + I_3 + I_4. \quad (\text{S15})$$

558 These quantities are used to compute the normalized distance from the attractor, as  
 559 described in the main text.

## 560 Resilience of a multistrain system.

561 We use a simple two-strain model to show that a multistrain host-pathogen system  
 562 that is coupled through cross immunity can be described by a single resilience value.  
 563 The model dynamics can be described as follows [24]:

$$\frac{dS}{dt} = \mu - \mu S - (\lambda_1 + \lambda_2)S + \rho_1 R_1 + \rho_2 R_2 \quad (\text{S16})$$

$$\frac{dI_1}{dt} = \lambda_1 S - (\gamma_1 + \mu)I_1 \quad (\text{S17})$$

$$\frac{dI_2}{dt} = \lambda_2 S - (\gamma_2 + \mu)I_2 \quad (\text{S18})$$

$$\frac{dR_1}{dt} = \gamma_1 I_1 - \lambda_2 \epsilon_{21} R_1 - \rho_1 R_1 + \rho_2 R - \mu R_1 \quad (\text{S19})$$

$$\frac{dR_2}{dt} = \gamma_2 I_2 - \lambda_1 \epsilon_{12} R_2 - \rho_2 R_2 + \rho_1 R - \mu R_2 \quad (\text{S20})$$

$$\frac{dJ_1}{dt} = \lambda_1 \epsilon_{12} R_2 - (\gamma_1 + \mu)J_1 \quad (\text{S21})$$

$$\frac{dJ_2}{dt} = \lambda_2 \epsilon_{21} R_1 - (\gamma_2 + \mu)J_2 \quad (\text{S22})$$

$$\frac{dR}{dt} = \gamma_1 J_1 + \gamma_2 J_2 - \rho_1 R - \rho_2 R - \mu R \quad (\text{S23})$$

564 where  $S$  represents the proportion of individuals who are fully susceptible to infections  
 565 by both strains;  $I_1$  represents the proportion of individuals who are infected with strain 1 without prior immunity;  $I_2$  represents the proportion of individuals who are infected with strain 2 without prior immunity;  $R_1$  represents the proportion of individuals who are fully immune against strain 1 and partially susceptible to reinfection by strain 2;  $R_2$  represents the proportion of individuals who are fully immune against strain 2 and partially susceptible to reinfection by strain 1;  $J_1$  represents the proportion of individuals who are infected with strain 1 with prior immunity against strain 2;  $J_2$  represents the proportion of individuals who are infected with strain 2 with prior immunity against strain 1;  $R$  represents the proportion of individuals who are immune to infections from both strains;  $\mu$  represents the birth/death rate;  
 566  $\lambda_1$  and  $\lambda_2$  represent the force of infection from strains 1 and 2, respectively;  $\rho_1$  and  
 567  $\rho_2$  represent the waning immunity rate;  $\gamma_1$  and  $\gamma_2$  represent the recovery rate;  $\epsilon_{21}$   
 568 and  $\epsilon_{12}$  represent the susceptibility to reinfection with strains 2 and 1, respectively,  
 569 given prior immunity from infection with strains 1 and 2, respectively. The force of  
 570 infection is modeled as follows:  
 571

$$\beta_1 = b_1(1 + \theta_1 \sin(2\pi(t - \phi_1)))\alpha(t) \quad (\text{S24})$$

$$\beta_2 = b_2(1 + \theta_2 \sin(2\pi(t - \phi_2)))\alpha(t) \quad (\text{S25})$$

$$\lambda_1 = \beta_1(I_1 + J_1) \quad (\text{S26})$$

$$\lambda_2 = \beta_2(I_2 + J_2) \quad (\text{S27})$$

580 In Supplementary Figures S2–S4, we assume the following parameters:  $b_1 = 2 \times$   
 581 52/years,  $b_2 = 4 \times 52/\text{years}$ ,  $\phi_1 = \phi_2 = 0$ ,  $\epsilon_{12} = 0.9$ ,  $\epsilon_{21} = 0.5$ ,  $\gamma_1 = \gamma_2 = 52/\text{years}$ ,  
 582  $\rho_1 = \rho_2 = 1/\text{years}$ , and  $\mu = 1/70/\text{years}$ . For all simulations, we assume a 50%  
 583 transmission reduction for 6 months from 2020:

$$\alpha(t) = \begin{cases} 0.5 & 2020 \leq t < 2020.5 \\ 1 & \text{otherwise} \end{cases} \quad (\text{S28})$$

584 The seasonal amplitude  $\theta$  is varied from 0 to 0.4. All simulations were ran from 1900  
 585 to 2030 with following initial conditions:  $S(0) = 1 - 2 \times 10^{-6}$ ,  $I_1(0) = 1 \times 10^{-6}$ ,  
 586  $I_2(0) = 1 \times 10^{-6}$ ,  $R_1(0) = 0$ ,  $R_2(0) = 0$ ,  $J_1(0) = 0$ ,  $J_2(0) = 0$ , and  $R(0) = 0$ .

587 We consider three scenarios for measuring pathogen resilience: (1) we only have  
 588 information about strain 1, (2) we only have information about strain 2, and (3)  
 589 we are unable to distinguish between strains. In the first two scenarios (see panels  
 590 A–C for strain 1 and panels D–F for strain 2), we consider the dynamics of average  
 591 susceptibility for each strain and total prevalence:

$$\bar{S}_1 = S + \epsilon_{12}R_2 \quad (\text{S29})$$

$$\hat{I}_1 = I_1 + J_1 \quad (\text{S30})$$

$$\bar{S}_2 = S + \epsilon_{21}R_1 \quad (\text{S31})$$

$$\hat{I}_2 = I_2 + J_2 \quad (\text{S32})$$

<sup>592</sup> In the third scenario (panels G–I), we consider the dynamics of total susceptible and  
<sup>593</sup> infected populations:

$$\hat{S} = S + R_2 + R_1 \quad (\text{S33})$$

$$\hat{I} = I_1 + J_1 + I_2 + J_2 \quad (\text{S34})$$

<sup>594</sup> These quantities are used to compute the normalized distance from the attractor, as  
<sup>595</sup> described in the main text.

## <sup>596</sup> Estimating intrinsic resilience using mechanistic model

<sup>597</sup> We tested whether we can reliably estimate the intrinsic resilience of a system by fit-  
<sup>598</sup> ting a mechanistic model. Specifically, we simulated case time series from stochastic  
<sup>599</sup> SIRS and two-strain models and fitted a simple, deterministic SIRS model using a  
<sup>600</sup> Bayesian framework.

<sup>601</sup> We simulated the models in discrete time, incorporating demographic stochastic-  
<sup>602</sup> ity:

$$\beta(t) = \mathcal{R}_0 \left( 1 + \theta \cos \left( \frac{2\pi t}{364} \right) \right) \alpha(t)(1 - \exp(-\gamma)) \quad (\text{S35})$$

$$\text{FOI}(t) = \beta(t)I(t - \Delta t)/N \quad (\text{S36})$$

$$B(t) \sim \text{Poisson}(\mu N) \quad (\text{S37})$$

$$\Delta S(t) \sim \text{Binom}(S(t - \Delta t), 1 - \exp(-(\text{FOI}(t) + \mu)\Delta t)) \quad (\text{S38})$$

$$N_{SI}(t) \sim \text{Binom}\left(\Delta S(t), \frac{\text{FOI}(t)}{\text{FOI}(t) + \mu}\right) \quad (\text{S39})$$

$$\Delta I(t) \sim \text{Binom}(I(t - \Delta t), 1 - \exp(-(\gamma + \mu)\Delta t)) \quad (\text{S40})$$

$$N_{IR}(t) \sim \text{Binom}\left(\Delta I(t), \frac{\gamma}{\gamma + \mu}\right) \quad (\text{S41})$$

$$\Delta R(t) \sim \text{Binom}(R(t - \Delta t), 1 - \exp(-(\delta + \mu)\Delta t)) \quad (\text{S42})$$

$$N_{RS}(t) \sim \text{Binom}\left(\Delta R(t), \frac{\delta}{\delta + \mu}\right) \quad (\text{S43})$$

$$S(t) = S(t - \Delta t) + N_{RS}(t) + B(t) - \Delta S(t) \quad (\text{S44})$$

$$I(t) = I(t - \Delta t) + N_{SI}(t) - \Delta I(t) \quad (\text{S45})$$

$$R(t) = R(t - \Delta t) + N_{IR}(t) - \Delta R(t) \quad (\text{S46})$$

<sup>603</sup> where FOI represent the force of infection;  $N_{ij}$  represent the number of individuals  
<sup>604</sup> moving from compartment  $i$  to  $j$  on a given day; and  $B(t)$  represents the number  
<sup>605</sup> of new births. We simulate the model on a daily scale—assuming 364 days in a  
<sup>606</sup> year so that it can be evenly grouped into 52 weeks—with the following parameters:  
<sup>607</sup>  $\mathcal{R}_0 = 3$ ,  $\theta = 0.1$ ,  $\gamma = 1/7/\text{days}$ ,  $\delta = 1/(364 \times 2)/\text{days}$ ,  $\mu = 1/(364 \times 50)/\text{days}$ , and  
<sup>608</sup>  $N = 1 \times 10^8$ . The model is simulated from 1900 to 2030 assuming  $S(0) = N/3$ ,

609  $I(0) = 100$ , and  $R(0) = N - S(0) - I(0)$ . The observed incidence from the model is  
610 then simulated as follows:

$$C(t) = \text{Beta-Binom}(N_{SI}(t), \rho, k), \quad (\text{S47})$$

611 where  $\rho$  represents the reporting probability and  $k$  represents the overdispersion pa-  
612 rameter of beta-binomial distribution. Here, we use the beta-binomial distribution to  
613 account for overdispersion in reporting. We assume  $\rho = 0.002$  (i.e., 0.2% probability)  
614 and  $k = 1000$ .

615 We used an analogous approach for the two-strain model:

$$\beta_1(t) = b_1 \left( 1 + \theta_1 \cos \left( \frac{2\pi(t - \phi_1)}{364} \right) \right) \alpha(t) \quad (\text{S48})$$

$$\beta_2(t) = b_2 \left( 1 + \theta_2 \cos \left( \frac{2\pi(t - \phi_2)}{364} \right) \right) \alpha(t) \quad (\text{S49})$$

$$\text{FOI}_1(t) = \beta_1(t)(I_1(t - \Delta t) + J_1(t - \Delta t))/N \quad (\text{S50})$$

$$\text{FOI}_2(t) = \beta_2(t)(I_2(t - \Delta t) + J_2(t - \Delta t))/N \quad (\text{S51})$$

$$B(t) \sim \text{Poisson}(\mu N) \quad (\text{S52})$$

$$\Delta S(t) \sim \text{Binom}(S(t - \Delta t), 1 - \exp(-(\text{FOI}_1(t) + \text{FOI}_2(t) + \mu)\Delta t)) \quad (\text{S53})$$

$$N_{SI_1}(t) \sim \text{Binom}\left(\Delta S(t), \frac{\text{FOI}_1(t)}{\text{FOI}_1(t) + \text{FOI}_2(t) + \mu}\right) \quad (\text{S54})$$

$$N_{SI_2}(t) \sim \text{Binom}\left(\Delta S(t), \frac{\text{FOI}_2(t)}{\text{FOI}_1(t) + \text{FOI}_2(t) + \mu}\right) \quad (\text{S55})$$

$$\Delta I_1(t) \sim \text{Binom}(I_1(t - \Delta t), 1 - \exp(-(\gamma_1 + \mu)\Delta t)) \quad (\text{S56})$$

$$N_{I_1 R_1}(t) \sim \text{Binom}\left(\Delta I_1(t), \frac{\gamma_1}{\gamma_1 + \mu}\right) \quad (\text{S57})$$

$$\Delta I_2(t) \sim \text{Binom}(I_2(t - \Delta t), 1 - \exp(-(\gamma_2 + \mu)\Delta t)) \quad (\text{S58})$$

$$N_{I_2 R_2}(t) \sim \text{Binom}\left(\Delta I_2(t), \frac{\gamma_2}{\gamma_2 + \mu}\right) \quad (\text{S59})$$

$$\Delta R_1(t) \sim \text{Binom}(R_1(t - \Delta t), 1 - \exp(-(\epsilon_{21}\text{FOI}_2(t) + \rho_1 + \mu)\Delta t)) \quad (\text{S60})$$

$$N_{R_1 S}(t) \sim \text{Binom}\left(\Delta R_1(t), \frac{\rho_1}{\epsilon_{21}\text{FOI}_2(t) + \rho_1 + \mu}\right) \quad (\text{S61})$$

$$N_{R_1 J_2}(t) \sim \text{Binom}\left(\Delta R_1(t), \frac{\epsilon_{21}\text{FOI}_2(t)}{\epsilon_{21}\text{FOI}_2(t) + \rho_1 + \mu}\right) \quad (\text{S62})$$

$$\Delta R_2(t) \sim \text{Binom}(R_2(t - \Delta t), 1 - \exp(-(\epsilon_{12}\text{FOI}_1(t) + \rho_2 + \mu)\Delta t)) \quad (\text{S63})$$

$$N_{R_2 S}(t) \sim \text{Binom}\left(\Delta R_2(t), \frac{\rho_2}{\epsilon_{12}\text{FOI}_1(t) + \rho_2 + \mu}\right) \quad (\text{S64})$$

$$N_{R_2 J_1}(t) \sim \text{Binom}\left(\Delta R_2(t), \frac{\epsilon_{12}\text{FOI}_1(t)}{\epsilon_{12}\text{FOI}_1(t) + \rho_2 + \mu}\right) \quad (\text{S65})$$

$$\Delta J_1(t) \sim \text{Binom}(J_1(t - \Delta t), 1 - \exp(-(\gamma_1 + \mu)\Delta t)) \quad (\text{S66})$$

$$N_{J_1R}(t) \sim \text{Binom}\left(\Delta J_1(t), \frac{\gamma_1}{\gamma_1 + \mu}\right) \quad (\text{S67})$$

$$\Delta J_2(t) \sim \text{Binom}(J_2(t - \Delta t), 1 - \exp(-(\gamma_2 + \mu)\Delta t)) \quad (\text{S68})$$

$$N_{J_2R}(t) \sim \text{Binom}\left(\Delta J_2(t), \frac{\gamma_2}{\gamma_2 + \mu}\right) \quad (\text{S69})$$

$$\Delta R(t) \sim \text{Binom}(R(t - \Delta t), 1 - \exp(-(\rho_1 + \rho_2 + \mu)\Delta t)) \quad (\text{S70})$$

$$N_{RR_1}(t) \sim \text{Binom}\left(\Delta R(t), \frac{\rho_1}{\rho_1 + \rho_2 + \mu}\right) \quad (\text{S71})$$

$$N_{RR_2}(t) \sim \text{Binom}\left(\Delta R(t), \frac{\rho_2}{\rho_1 + \rho_2 + \mu}\right) \quad (\text{S72})$$

$$S(t) = S(t - \Delta t) - \Delta S(t) + B(t) + N_{R_1S}(t) + N_{R_2S}(t) \quad (\text{S73})$$

$$I_1(t) = I_1(t - \Delta t) - \Delta I_1(t) + N_{SI_1}(t) \quad (\text{S74})$$

$$I_2(t) = I_2(t - \Delta t) - \Delta I_2(t) + N_{SI_2}(t) \quad (\text{S75})$$

$$R_1(t) = R_1(t - \Delta t) - \Delta R_1(t) + N_{I_1R_1}(t) + N_{RR_1}(t) \quad (\text{S76})$$

$$R_2(t) = R_2(t - \Delta t) - \Delta R_2(t) + N_{I_2R_2}(t) + N_{RR_2}(t) \quad (\text{S77})$$

$$J_1(t) = J_1(t - \Delta t) - \Delta J_1(t) + N_{R_2J_1}(t) \quad (\text{S78})$$

$$J_2(t) = J_2(t - \Delta t) - \Delta J_2(t) + N_{R_1J_2}(t) \quad (\text{S79})$$

$$R(t) = R(t - \Delta t) - \Delta R(t) + N_{J_1R}(t) + N_{J_2R}(t) \quad (\text{S80})$$

We simulate the model on a daily scale with previously estimated parameters for the RSV-HMPV interaction [24]:  $b_1 = 1.7/\text{weeks}$ ,  $b_2 = 1.95/\text{weeks}$ ,  $\theta_1 = 0.4$ ,  $\theta_2 = 0.3$ ,  $\phi_1 = 0.005 \times 7/364$ ,  $\phi_2 = 4.99 \times 7/364$ ,  $\epsilon_{12} = 0.92$ ,  $\epsilon_{21} = 0.45$ ,  $\gamma_1 = 1/10/\text{days}$ ,  $\gamma_2 = 1/10/\text{days}$ ,  $\rho_1 = 1/364/\text{days}$ ,  $\rho_2 = 1/364/\text{days}$ ,  $\mu = 1/(70 \times 364)/\text{days}$ , and  $N = 1 \times 10^8$ . The model is simulated from 1900 to 2030 assuming  $S(0) = N - 200$ ,  $I_1(0) = 100$ ,  $I_2(0) = 100$ ,  $R_1(0) = 0$ ,  $R_2(0) = 0$ ,  $J_1(0) = 0$ ,  $J_2(0) = 0$ , and  $R(0) = 0$ . The observed incidence for each strain is then simulated as follows:

$$C_1(t) = \text{Beta} - \text{Binom}(N_{SI_1}(t) + N_{R_2J_1}, \rho, k), \quad (\text{S81})$$

$$C_2(t) = \text{Beta} - \text{Binom}(N_{SI_2}(t) + N_{R_1J_2}, \rho, k), \quad (\text{S82})$$

where  $\rho$  represents the reporting probability and  $k$  represents the overdispersion parameter of beta-binomial distribution. We assume  $\rho = 0.002$  (i.e., 0.2% probability) and  $k = 500$ . We also consider the total incidence:  $C_{\text{total}}(t) = C_1(t) + C_2(t)$ .

For both models, we consider a more realistic challenges in intervention effects  $\alpha(t)$  to challenge our ability to estimate the intervention effects. Thus, we assume a 40% transmission reduction for 3 months from March 2020, followed by a 10% transmission reduction for 6 months, 20% transmission reduction for 3 months, and

630 a final return to normal levels:

$$\alpha(t) = \begin{cases} 1 & t < 2020.25 \\ 0.6 & 2020.25 \leq t < 2020.5 \\ 0.9 & 2020.5 \leq t < 2021 \\ 0.8 & 2021 \leq t < 2021.25 \\ 1 & 2021.25 \leq t \end{cases}. \quad (\text{S83})$$

631 For all simulations, we truncate the time series from the beginning of 2014 to the  
632 end of 2023 and aggregate them into weekly cases.

633 To infer intrinsic resilience from time series, we fit a simple discrete time, deter-  
634 ministic SIRS model [4]:

$$\Delta t = 1 \text{ week} \quad (\text{S84})$$

$$\text{FOI}(t) = \beta(t)(I(t - \Delta t) + \omega)/N \quad (\text{S85})$$

$$\Delta S(t) = [1 - \exp(-(\text{FOI}(t) + \mu)\Delta t)] S(t - \Delta t) \quad (\text{S86})$$

$$N_{SI}(t) = \frac{\text{FOI}(t)\Delta S(t)}{\text{FOI}(t) + \mu} \quad (\text{S87})$$

$$\Delta I(t) = [1 - \exp(-(\gamma + \mu)\Delta t)] I(t - \Delta t) \quad (\text{S88})$$

$$N_{IR}(t) = \frac{\gamma \Delta I(t)}{\gamma + \mu} \quad (\text{S89})$$

$$\Delta R(t) = [1 - \exp(-(\nu + \mu)\Delta t)] R(t - \Delta t) \quad (\text{S90})$$

$$N_{RS}(t) = \frac{\nu \Delta R(t)}{\nu + \mu} \quad (\text{S91})$$

$$S(t) = S(t - \Delta t) + \mu S - \Delta S(t) + N_{RS}(t) \quad (\text{S92})$$

$$I(t) = I(t - \Delta t) - \Delta I(t) + N_{SI}(t) \quad (\text{S93})$$

$$R(t) = R(t - \Delta t) - \Delta R(t) + N_{IR}(t) \quad (\text{S94})$$

635 where we include an extra term  $\omega$  to account for external infections. Although actual  
636 simulations do not include any external infections, we found that including this term  
637 generally helped with model convergence in previous analyses [4]. The transmission  
638 rate is divided into a seasonal term  $\beta_{\text{seas}}(t)$  (repeated every year) and intervention  
639 term  $\alpha(t)$ , which are estimated jointly:

$$\beta(t) = \beta_{\text{seas}}(t)\alpha(t), \quad (\text{S95})$$

640 where  $\alpha < 1$  corresponds to reduction in transmission due to intervention effects. To  
641 constrain the smoothness of  $\beta_{\text{seas}}(t)$ , we impose cyclic, random-walk priors:

$$\beta_{\text{seas}}(t) \sim \text{Normal}(\beta_{\text{seas}}(t - 1), \sigma) \quad t = 2 \dots 52 \quad (\text{S96})$$

$$\beta_{\text{seas}}(1) \sim \text{Normal}(\beta_{\text{seas}}(52), \sigma) \quad (\text{S97})$$

642 [SWP: I noticed that I forgot to put a prior on  $\sigma$  so need to re-do this but won't  
 643 change the results.] We fix  $\alpha(t) = 1$  for all  $t < 2020$  and estimate  $\alpha$  assuming a  
 644 normal prior:

$$\alpha \sim \text{Normal}(1, 0.25). \quad (\text{S98})$$

645 We assume weakly informative priors on  $\omega$  and  $\nu$ :

$$\omega \sim \text{Normal}(0, 200) \quad (\text{S99})$$

$$\nu \sim \text{Normal}(104, 26) \quad (\text{S100})$$

646 We assume that the true birth/death rates, population sizes, and recovery rates are  
 647 known. We note, however, that assuming  $\gamma = 1/\text{week}$  actually corresponds to a  
 648 mean simulated infectious period of 1.6 weeks, which is much longer than the true  
 649 value; this approximation allows us to test whether we can still robustly estimate the  
 650 intrinsic resilience given parameter mis-specification. Initial conditions are estimated  
 651 with following priors:

$$S(0) = Ns(0) \quad (\text{S101})$$

$$I(0) = Ni(0) \quad (\text{S102})$$

$$s(0) \sim \text{Uniform}(0, 1) \quad (\text{S103})$$

$$i(0) \sim \text{Half-Normal}(0, 0.001) \quad (\text{S104})$$

652 Finally, the Observation model is specified as follows:

$$\text{Cases}(t) \sim \text{Negative-Binomial}(\rho N_{SI}(t), \phi) \quad (\text{S105})$$

$$\rho \sim \text{Half-Normal}(0, 0.02) \quad (\text{S106})$$

$$\phi \sim \text{Half-Normal}(0, 10) \quad (\text{S107})$$

653 where  $\rho$  represents the reporting probability and  $\phi$  represents the negative binomial  
 654 overdispersion parameter.

655 The model is fitted to four separate time series: (1) incidence time series from  
 656 the SIRS model, (2) incidence time series for strain 1 from the two-strain model,  
 657 (3) incidence time series for strain 2 from the two-strain model, and (4) combined  
 658 incidence time series for strains 1 and 2 from the two-strain model. The model was  
 659 fitted using rstan [33, 34]. The resulting posterior distribution was used to calculate  
 660 the intrinsic resilience of the seasonally unforced system with the same parameters;  
 661 eigenvalues of the discrete-time SIR model were computed by numerically finding  
 662 the equilibrium and calculating the Jacobian matrix.

## 663 Validations for window-selection criteria

664 We use stochastic SIRS simulations to validate the window-selection criteria that we  
 665 use for the linear regression for estimating empirical resilience. For each simulation,  
 666 we begin by generating a random intervention  $\alpha(t)$  from a random set of parameters.

667 First, we draw the duration of intervention  $\tau_{\text{npi}}$  from a uniform distribution between  
 668 0.5 and 3.5 years. Then, we draw independent normal variables  $z_i$  of length  $\lfloor 364\tau_{\text{npi}} \rfloor$   
 669 with a standard deviation of 0.02 and take a reverse cumulative sum to obtain a  
 670 realistic shape for the intervention:

$$x_n = 1 + \sum_{i=n}^{\lfloor 364\tau_{\text{npi}} \rfloor} z_i, \quad n = 1, \dots, \lfloor 364\tau_{\text{npi}} \rfloor. \quad (\text{S108})$$

671 We repeat this random generation process until less than 10% of  $x_n$  exceeds 1. Then,  
 672 we set any values that are above 1 or below 0 as 1 and 0, respectively. Then, we  
 673 randomly draw the minimum transmission during intervention  $\alpha_{\min}$  from a uniform  
 674 distribution between 0.5 and 0.7 and scale  $x_n$  to have a minimum of  $\alpha_{\min}$ :

$$x_{\text{scale},n} = \alpha_{\min} + (1 - \alpha_{\min}) \times \frac{x_n - \min x_n}{1 - \min x_n}. \quad (\text{S109})$$

675 This allows us to simulate a realistically shaped intervention:

$$\alpha(t) = \begin{cases} 1 & t < 2020 \\ x_{\text{scale},364(t-2020)} & 2020 \leq t < 2020 + \tau_{\text{npi}} \\ 1 & \tau_{\text{npi}} \leq t \end{cases}. \quad (\text{S110})$$

676 Given this intervention function, we draw  $\mathcal{R}_0$  from a uniform distribution between 1.5  
 677 and 3 and the mean duration of immunity  $1/\delta$  from a uniform distribution between  
 678 0.5 and 2. Then, we simulate the stochastic SIRS model from  $S(0) = 10^8/\mathcal{R}_0$  and  
 679  $I(0) = 100$  from 1990 to 2025 and truncate the time series to 2014–2025; if the  
 680 epidemic becomes extinct before the end of simulation, we discard that simulation  
 681 and start over from the intervention generation step. We then apply the window  
 682 selection criteria described in the main text to compute the empirical resilience and  
 683 compare it against the intrinsic resilience of the seasonally unforced system. We also  
 684 compare this with the naive approach that uses the entire distance-from-attractor  
 685 time series, starting from the maximum distance. We repeat this procedure 500  
 686 times and quantify the correlation between empirical and intrinsic resilience estimates  
 687 across two approaches.

# Supplementary Figures

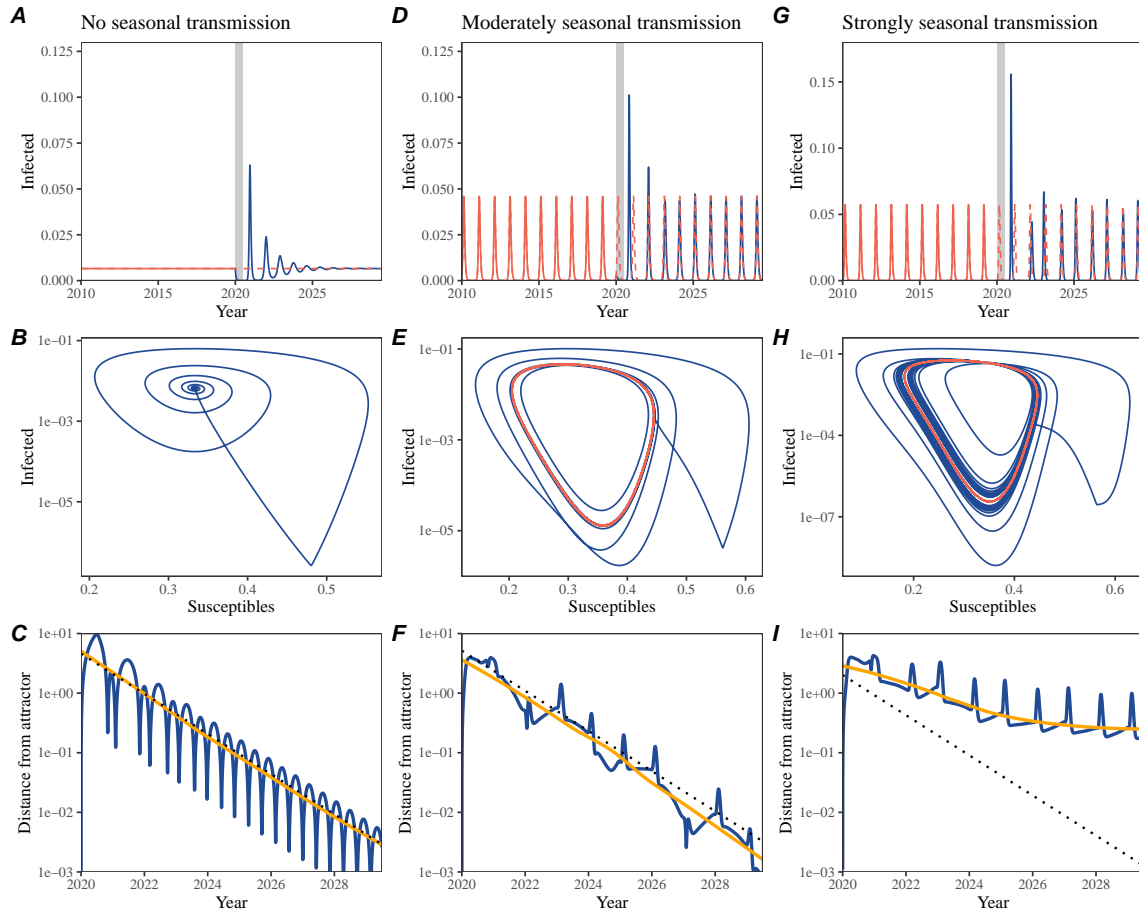


**Figure S1: Impact of seasonal transmission on pathogen resilience.** (A, D, G) Simulated epidemic trajectories using the SIRS model without seasonal forcing (A), with seasonal forcing of amplitude of 0.2 (D), and with seasonal forcing of amplitude of 0.4 (G). Red and blue solid lines represent epidemic dynamics before and after interventions are introduced, respectively. Red dashed lines represent counterfactual epidemic dynamics in the absence of interventions. Gray regions indicate the duration of interventions. (B, E, H) Phase plane representation of the corresponding model. Red and blue solid lines represent epidemic trajectories on an SI phase plane before and after interventions are introduced, respectively. (C, F, I) Changes in logged distance from the attractor over time. Blue lines represent the logged distance from the attractor. Orange lines represent the locally estimated scatterplot smoothing (LOESS) fits to the logged distance from the attractor. Dotted lines are superimposed as a comparison to have the same slope as the intrinsic resilience of the seasonally unforced system.

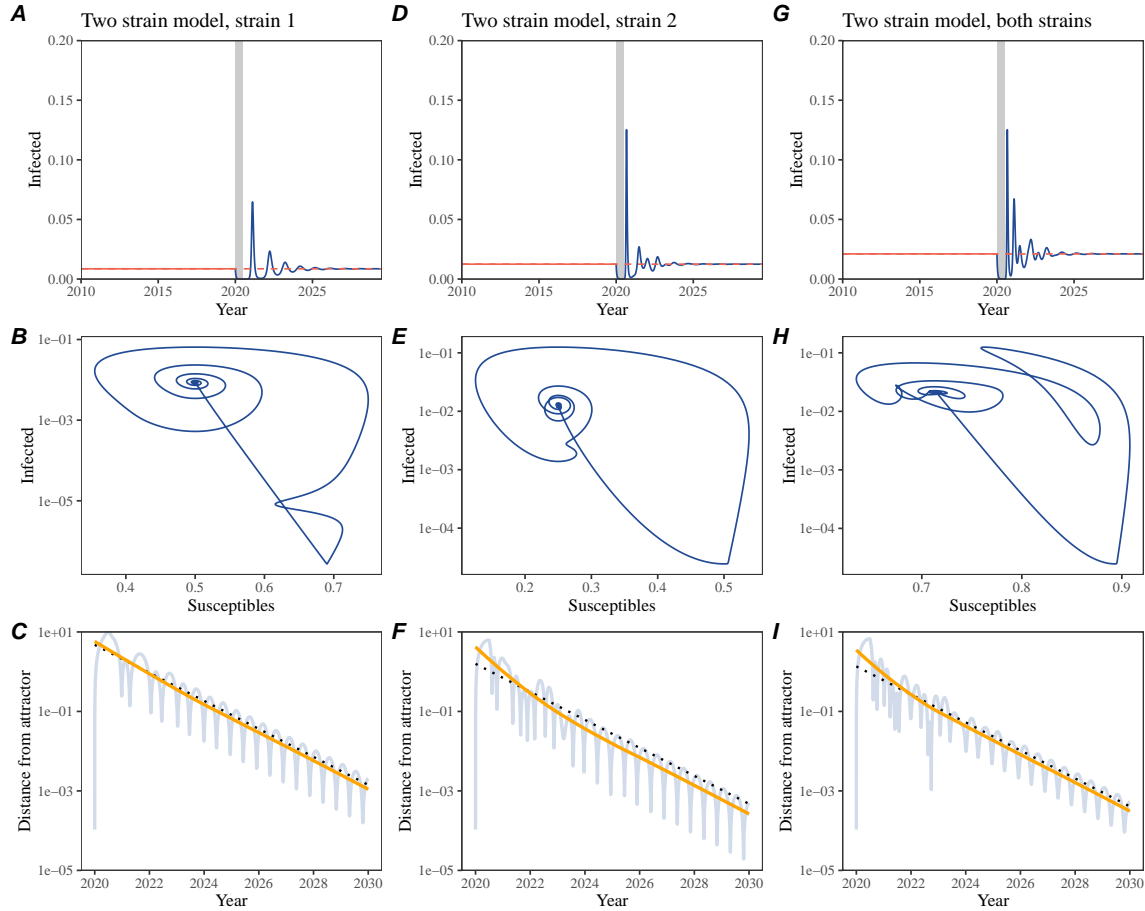


**Figure S2: Conceptual framework for measuring pathogen resilience following NPIs for a two-strain system without seasonal forcing.** (A, D, G) Simulated epidemic trajectories using a multi-strain system without seasonal forcing. Red and blue solid lines represent epidemic dynamics before and after interventions are introduced, respectively. Red dashed lines represent counterfactual epidemic dynamics in the absence of interventions. Gray regions indicate the duration of interventions. (B, E, H) Phase plane representation of the corresponding model. Blue solid lines represent epidemic trajectories on an SI phase plane before and after interventions are introduced, respectively. (C, F, I) Changes in logged distance from the attractor over time. Blue lines represent the logged distance from the attractor. Orange lines represent the locally estimated scatterplot smoothing (LOESS) fits to the logged distance from the attractor. Dotted lines are superimposed as a comparison to have the same slope as the intrinsic resilience of the seasonally unforced system.

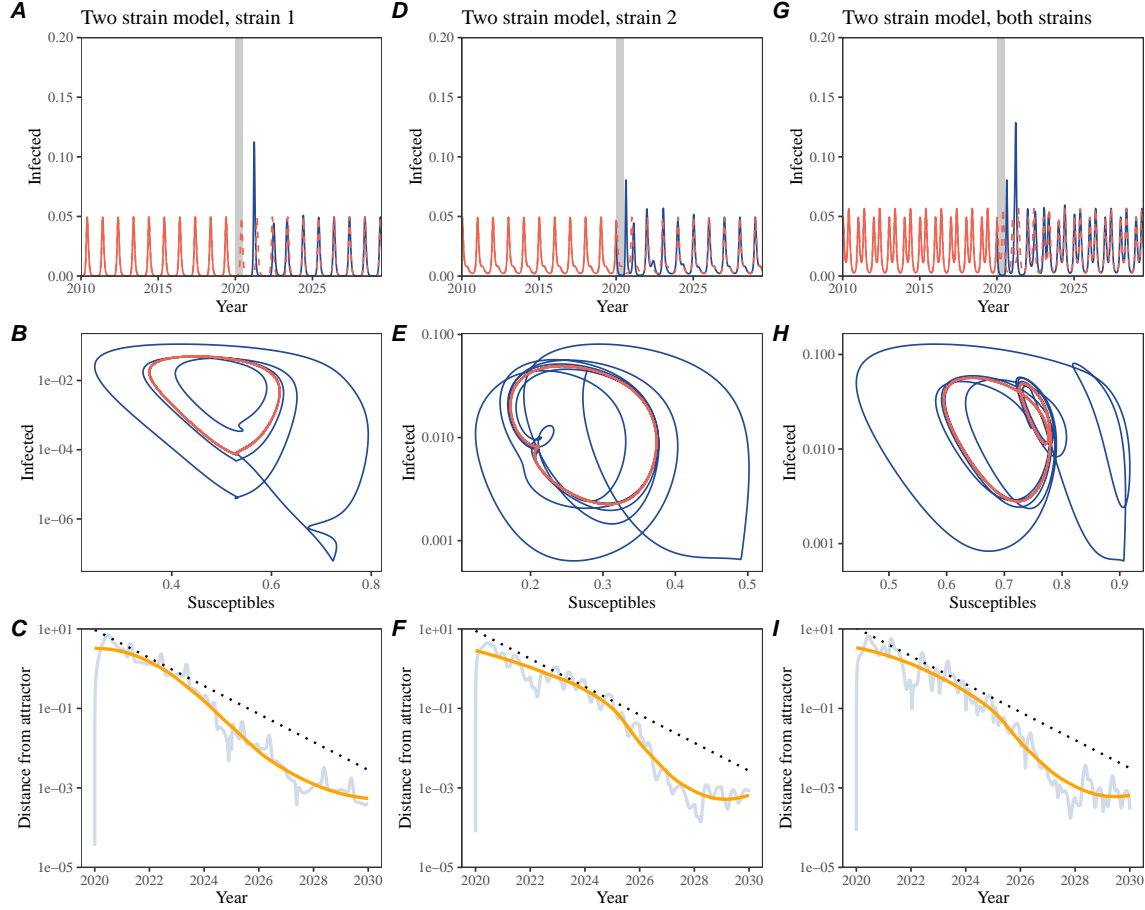


**Figure S3: Conceptual framework for measuring pathogen resilience following NPIs for a multi-strain system with seasonal forcing.** (A, D, G) Simulated epidemic trajectories using a multi-strain system with seasonal forcing (amplitude of 0.2). Red and blue solid lines represent epidemic dynamics before and after interventions are introduced, respectively. Red dashed lines represent counterfactual epidemic dynamics in the absence of interventions. Gray regions indicate the duration of interventions. (B, E, H) Phase plane representation of the corresponding model. Red and blue solid lines represent epidemic trajectories on an SI phase plane before and after interventions are introduced, respectively. (C, F, I) Changes in logged distance from the attractor over time. Blue lines represent the logged distance from the attractor. Orange lines represent the locally estimated scatterplot smoothing (LOESS) fits to the logged distance from the attractor. Dotted lines are superimposed as a comparison to have the same slope as the intrinsic resilience of the seasonally unforced system.

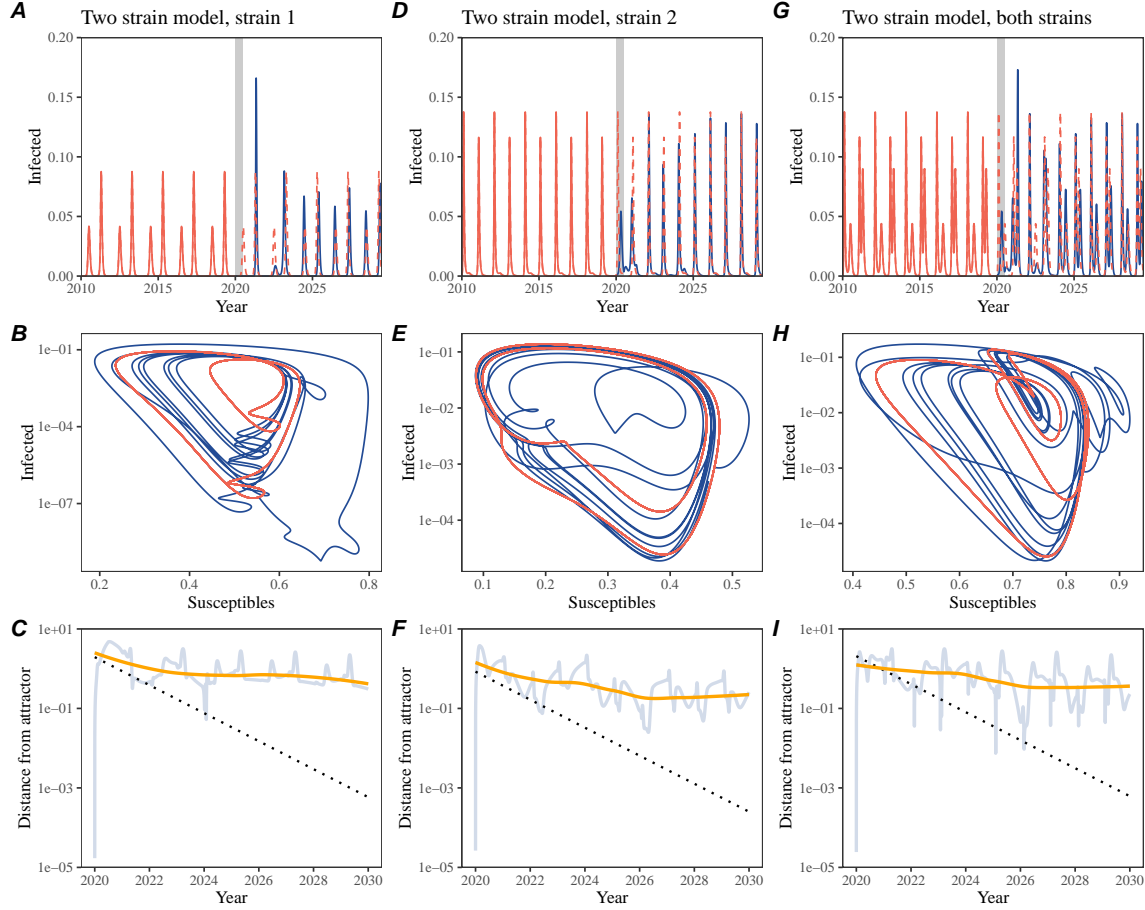


**Figure S4: Conceptual framework for measuring pathogen resilience following NPIs for a multi-strain system with strong seasonal forcing.** (A, D, G) Simulated epidemic trajectories using a multi-strain system with seasonal forcing (amplitude of 0.4). Red and blue solid lines represent epidemic dynamics before and after interventions are introduced, respectively. Red dashed lines represent counterfactual epidemic dynamics in the absence of interventions. Gray regions indicate the duration of interventions. (B, E, H) Phase plane representation of the corresponding model. Red and blue solid lines represent epidemic trajectories on an SI phase plane before and after interventions are introduced, respectively. (C, F, I) Changes in logged distance from the attractor over time. Blue lines represent the logged distance from the attractor. Orange lines represent the locally estimated scatterplot smoothing (LOESS) fits to the logged distance from the attractor. Dotted lines are superimposed as a comparison to have the same slope as the intrinsic resilience of the seasonally unforced system.

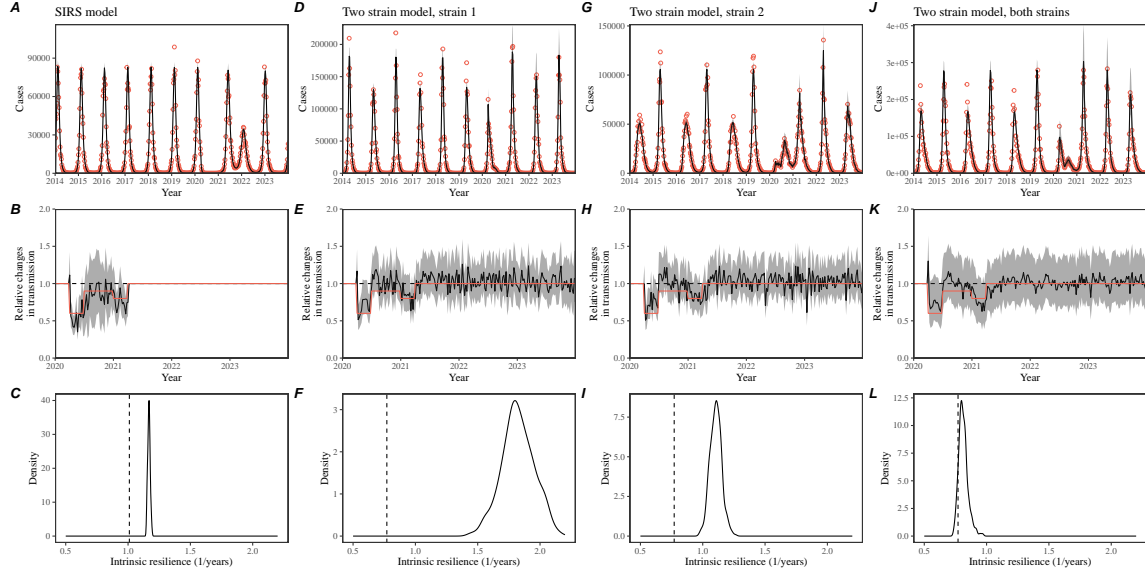


**Figure S5: Mechanistic model fits to simulated data and inferred intrinsic resilience.** (A, D, G, J) Simulated case time series from corresponding models (red) and SIRS model fits (black). (B, E, H, K) Assumed changes in transmission due to pandemic NPIs (red) and estimated changes from the SIRS model (black). Solid lines and shaded regions represent fitted posterior median and 95% credible intervals. (C, F, I, L) True intrinsic resilience of the seasonally unforced system (vertical lines) and the posterior distribution of the inferred intrinsic resilience from the SIRS model (density plots).

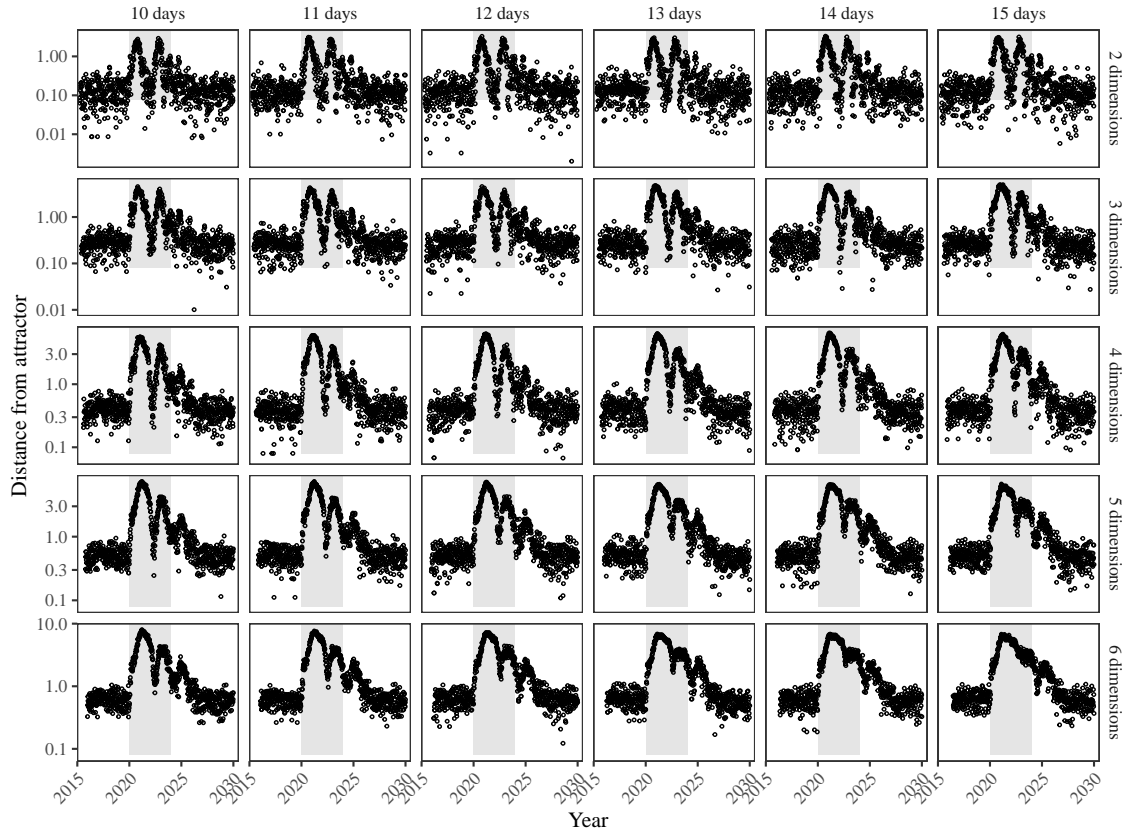


**Figure S6: Sensitivity of the distance from the attractor to choices about embedding lags and dimensions.** Sensitivity analysis for the distance-from-attractor time series shown in Figure 3E in the main text by varying the embedding lag between 10–15 days and embedding dimensions between 2–6 dimensions.

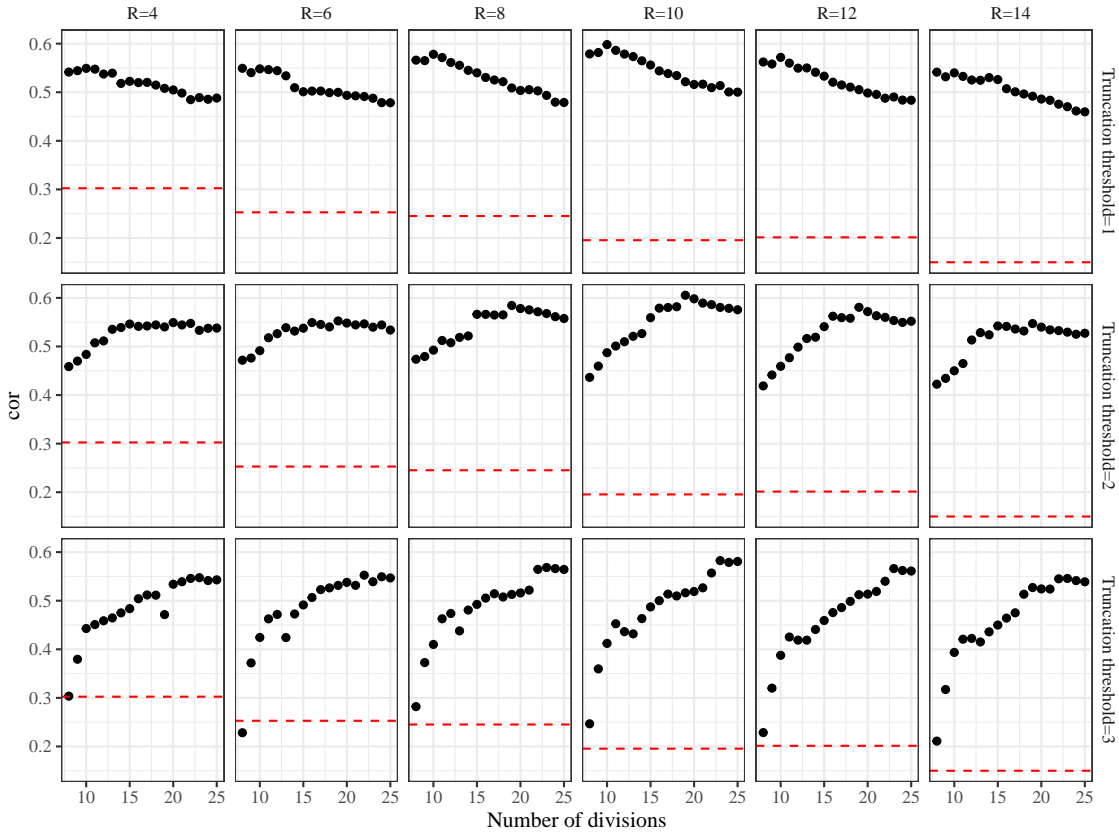


**Figure S7: Impact of fitting window selection on the estimation of empirical resilience.** We simulated 500 epidemics of a stochastic SIRS model with randomly drawn parameters and randomly generated intervention impacts. For each simulation, we reconstructed the empirical attractor based on the approach outlined in Figure 3 and estimate the distance from the attractor. The naive approach fits a linear regression on a log scale, starting from the maximum distance until the end of the time series. The window-based approach tries to select an appropriate window by smoothing the distance estimates and finding the time period when the smoothed time series crosses pre-determined threshold, relative to the maximum distance; then, a linear regression is fitted by using the raw distance within this time period.

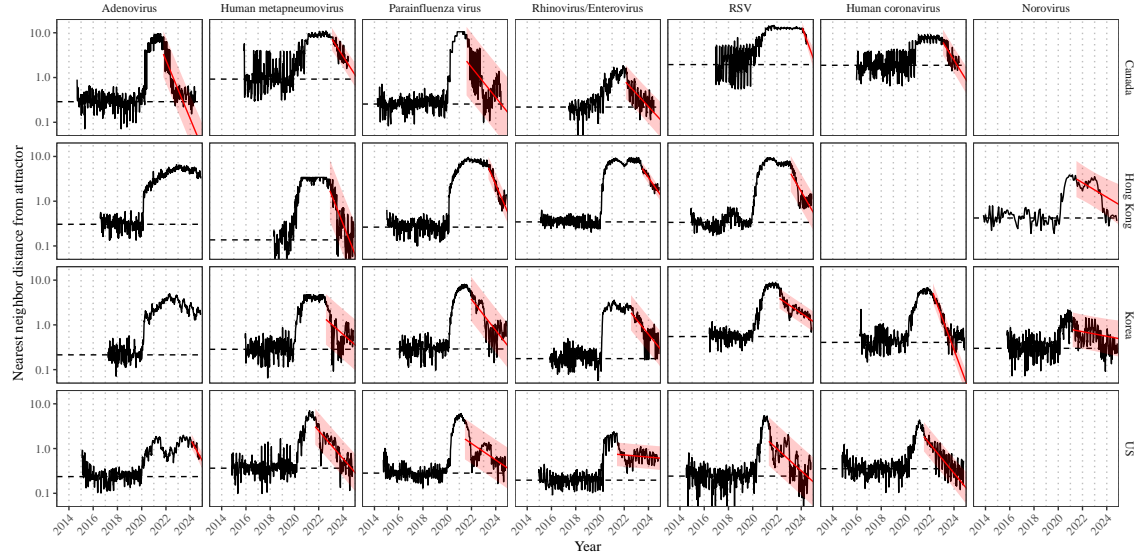


**Figure S8: Estimated time series of distance from the attractor for each pathogen and corresponding linear regression fits using automated window selection criterion across Canada, Hong Kong, Korea, and the US.** Black lines represent the estimated distance from the attractor. Red lines and shaded regions represent the linear regression fits and corresponding 95% confidence intervals. Dashed lines represent the average of the pre-pandemic nearest neighbor distances.

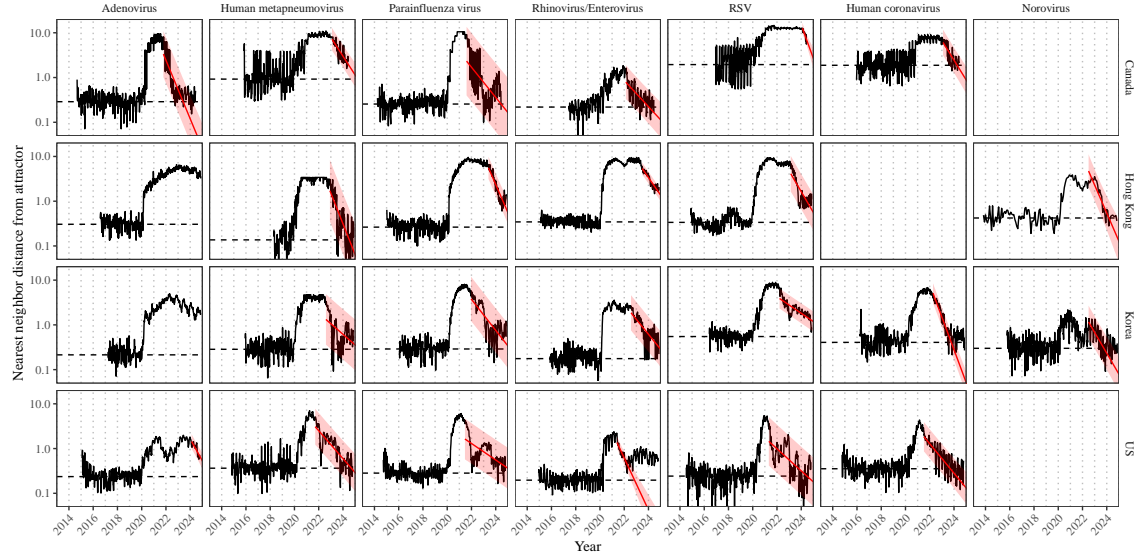


**Figure S9: Estimated time series of distance from the attractor for each pathogen and corresponding linear regression fits across Canada, Hong Kong, Korea, and the US, including ad-hoc regression window selection.** We used ad-hoc regression windows for norovirus in Hong Kong and Korea and Rhinovirus/Enterovirus in the US. Black lines represent the estimated distance from the attractor. Red lines and shaded regions represent the linear regression fits and corresponding 95% confidence intervals. Dashed lines represent the average of the pre-pandemic nearest neighbor distances.

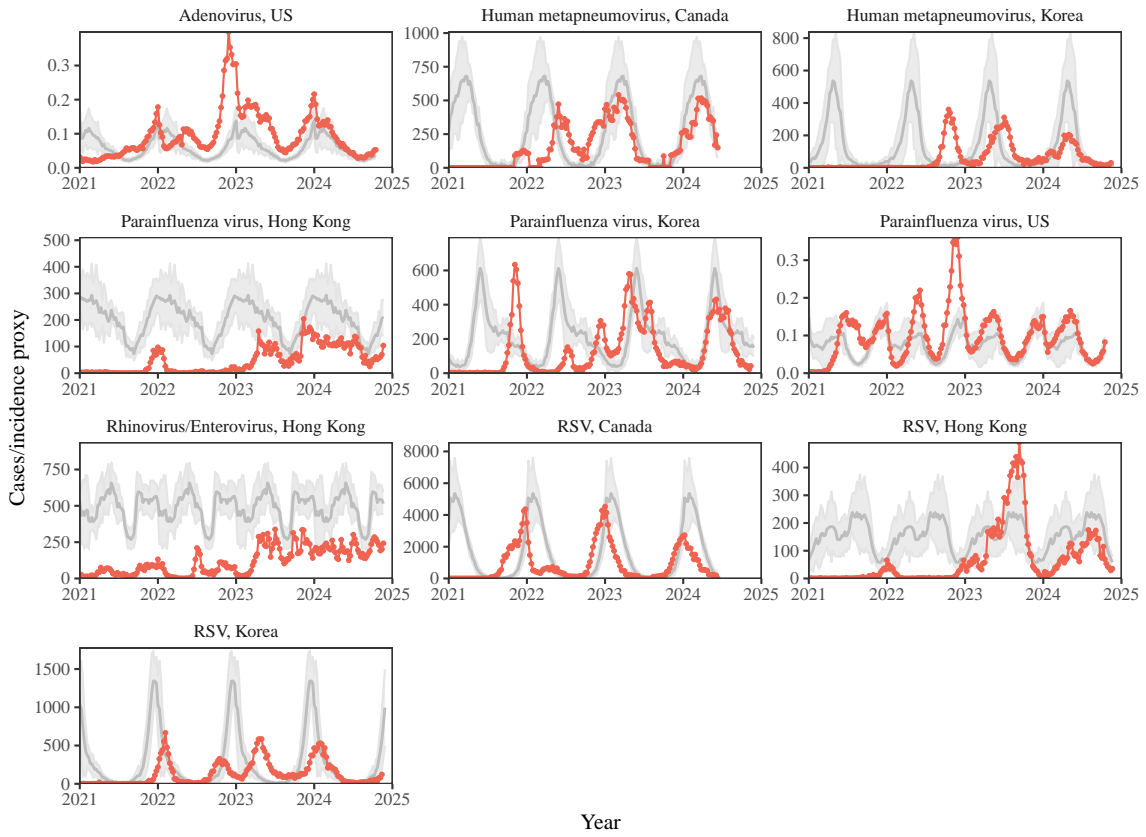


**Figure S10: Observed dynamics for pathogen that are predicted to return after the end of 2024.** Red points and lines represent data before 2020. Gray lines and shaded regions represent the mean seasonal patterns and corresponding 95% confidence intervals around the mean, previously shown in Figure 1.

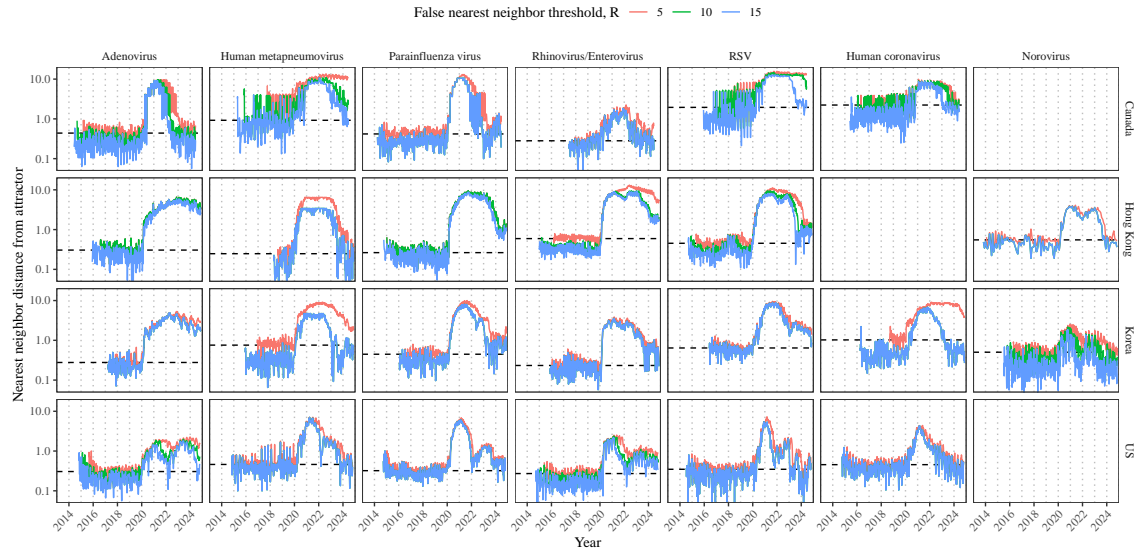


**Figure S11: Estimated time series of distance from the attractor for each pathogen across different choices about false nearest neighbor threshold values.** Using higher threshold values for the false nearest neighbor approach gives lower embedding dimensions. Colored lines represent the estimated distance from the attractor for different threshold values.

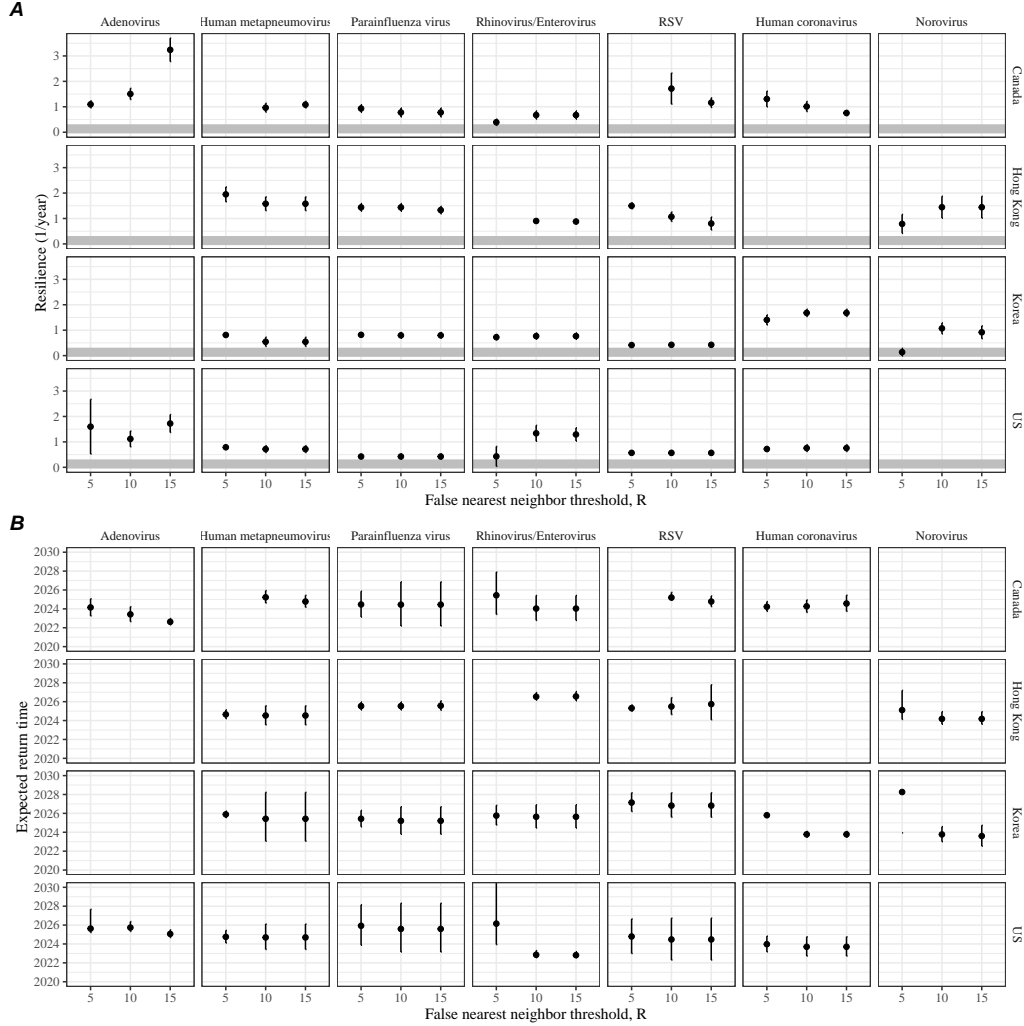


**Figure S12: Summary of resilience estimates and predictions for return time across different choices about false nearest neighbor threshold values.** The automated window selection method was used for all scenarios to estimate pathogen resilience, except for norovirus in Hong Kong and Korea and Rhinovirus/Enterovirus in the US. We used the same ad-hoc regression windows for norovirus in Hong Kong and Korea and Rhinovirus/Enterovirus in the US as we did in the main analysis. (A) Estimated pathogen resilience. The gray horizontal line represents the intrinsic resilience of pre-vaccination measles dynamics. (B) Predicted timing of when each pathogen will return to their pre-pandemic cycles. The dashed line in panel B indicates the end of 2024 (current observation time). Error bars represent 95% confidence intervals.

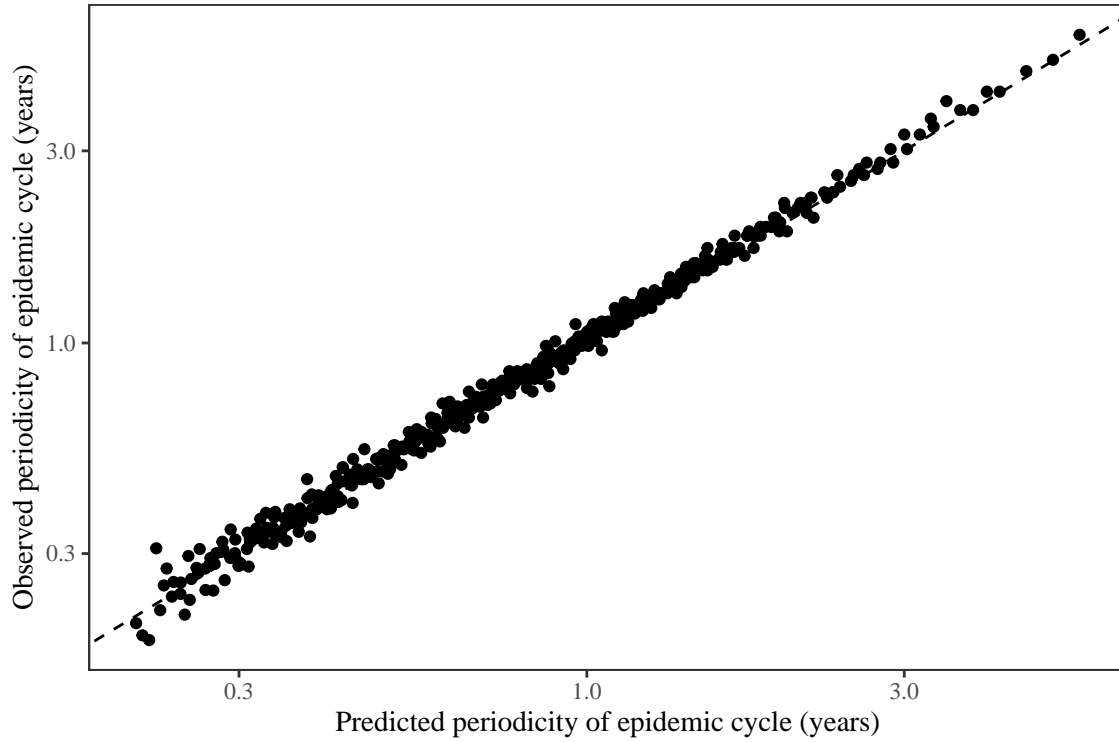
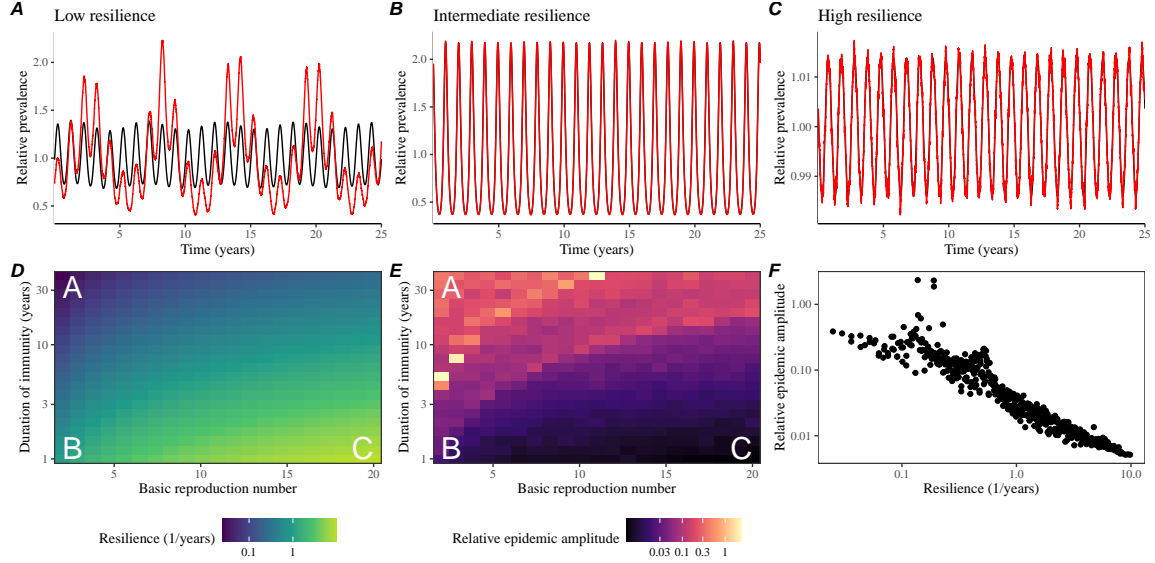


Figure S13: **Comparison between the observed and predicted periodicity of the epidemic cycle of the seasonally unforced SIRS model.** The observed periodicity of the epidemic corresponds to the periodicity at which maximum spectral density occurs. The predicted periodicity of the epidemic corresponds to  $2\pi/\text{Im}(\lambda)$ , where  $\text{Im}(\lambda)$  is the imaginary part of the eigenvalue.



**Figure S14: Linking resilience of a host-pathogen system to its sensitivity to stochastic perturbations for the seasonally forced SIRS model.** (A–C) Epidemic trajectories of a stochastic SIRS model across three different resilience values: low, intermediate, and high. The relative prevalence was calculated by dividing infection prevalence by its mean value. (D) The heat map represents the intrinsic resilience of the seasonally unforced system as a function of the basic reproduction number  $\mathcal{R}_0$  and the duration of immunity. (E) The heat map represents the relative epidemic amplitude as a function of the basic reproduction number  $\mathcal{R}_0$  and the duration of immunity. To calculate the relative epidemic amplitude, we first take the relative difference in infection prevalence between stochastic and deterministic trajectories:  $\epsilon = (I_{\text{stoch}} - I_{\text{det}})/I_{\text{det}}$ . Then, we calculate the difference between maximum and minimum of the relative difference and divide by half:  $(\max \epsilon - \min \epsilon)/2$ . (F) The relationship between pathogen resilience and relative epidemic amplitude.

## 689 References

- 690 [1] Rachel E Baker, Sang Woo Park, Wenchang Yang, Gabriel A Vecchi, C Jessica E  
691 Metcalf, and Bryan T Grenfell. The impact of COVID-19 nonpharmaceutical  
692 interventions on the future dynamics of endemic infections. *Proceedings of the*  
693 *National Academy of Sciences*, 117(48):30547–30553, 2020.
- 694 [2] Gabriela B Gomez, Cedric Mahé, and Sandra S Chaves. Uncertain effects of the  
695 pandemic on respiratory viruses. *Science*, 372(6546):1043–1044, 2021.
- 696 [3] Mihaly Koltai, Fabienne Krauer, David Hodgson, Edwin van Leeuwen, Marina  
697 Treskova-Schwarzbach, Mark Jit, and Stefan Flasche. Determinants of RSV  
698 epidemiology following suppression through pandemic contact restrictions. *Epi-*  
699 *demics*, 40:100614, 2022.
- 700 [4] Sang Woo Park, Brooklyn Noble, Emily Howerton, Bjarke F Nielsen, Sarah  
701 Lentz, Lilliam Ambroggio, Samuel Dominguez, Kevin Messacar, and Bryan T  
702 Grenfell. Predicting the impact of non-pharmaceutical interventions against  
703 COVID-19 on *Mycoplasma pneumoniae* in the United States. *Epidemics*,  
704 49:100808, 2024.
- 705 [5] Amanda C Perofsky, Chelsea L Hansen, Roy Burstein, Shanda Boyle, Robin  
706 Prentice, Cooper Marshall, David Reinhart, Ben Capodanno, Melissa Truong,  
707 Kristen Schwabe-Fry, et al. Impacts of human mobility on the citywide trans-  
708 mission dynamics of 18 respiratory viruses in pre-and post-COVID-19 pandemic  
709 years. *Nature communications*, 15(1):4164, 2024.
- 710 [6] Eric J Chow, Timothy M Uyeki, and Helen Y Chu. The effects of the COVID-19  
711 pandemic on community respiratory virus activity. *Nature Reviews Microbiol-*  
712 *ogy*, 21(3):195–210, 2023.
- 713 [7] Stephen M Kissler, Christine Tedijanto, Edward Goldstein, Yonatan H Grad,  
714 and Marc Lipsitch. Projecting the transmission dynamics of SARS-CoV-2  
715 through the postpandemic period. *Science*, 368(6493):860–868, 2020.
- 716 [8] Rachel E Baker, Chadi M Saad-Roy, Sang Woo Park, Jeremy Farrar, C Jessica E  
717 Metcalf, and Bryan T Grenfell. Long-term benefits of nonpharmaceutical inter-  
718 ventions for endemic infections are shaped by respiratory pathogen dynamics.  
719 *Proceedings of the National Academy of Sciences*, 119(49):e2208895119, 2022.
- 720 [9] John-Sebastian Eden, Chisha Sikazwe, Ruopeng Xie, Yi-Mo Deng, Sheena G  
721 Sullivan, Alice Michie, Avram Levy, Elena Cutmore, Christopher C Blyth,  
722 Philip N Britton, et al. Off-season RSV epidemics in Australia after easing  
723 of COVID-19 restrictions. *Nature communications*, 13(1):2884, 2022.
- 724 [10] Stuart L Pimm. The structure of food webs. *Theoretical population biology*,  
725 16(2):144–158, 1979.

- 726 [11] Michael G Neubert and Hal Caswell. Alternatives to resilience for measuring  
727 the responses of ecological systems to perturbations. *Ecology*, 78(3):653–665,  
728 1997.
- 729 [12] Lance H Gunderson. Ecological resilience—in theory and application. *Annual  
730 review of ecology and systematics*, 31(1):425–439, 2000.
- 731 [13] Vasilis Dakos and Sonia Kéfi. Ecological resilience: what to measure and how.  
732 *Environmental Research Letters*, 17(4):043003, 2022.
- 733 [14] Floris Takens. Detecting strange attractors in turbulence. In *Dynamical Sys-  
734 tems and Turbulence, Warwick 1980: proceedings of a symposium held at the  
735 University of Warwick 1979/80*, pages 366–381. Springer, 2006.
- 736 [15] Jonathan Dushoff, Joshua B Plotkin, Simon A Levin, and David JD Earn. Dynamical resonance can account for seasonality of influenza epidemics. *Pro-  
737 ceedings of the National Academy of Sciences*, 101(48):16915–16916, 2004.
- 739 [16] Alan Hastings, Karen C Abbott, Kim Cuddington, Tessa Francis, Gabriel Gell-  
740 ner, Ying-Cheng Lai, Andrew Morozov, Sergei Petrovskii, Katherine Scran-  
741 ton, and Mary Lou Zeeman. Transient phenomena in ecology. *Science*,  
742 361(6406):eaat6412, 2018.
- 743 [17] Matthew B Kennel, Reggie Brown, and Henry DI Abarbanel. Determining  
744 embedding dimension for phase-space reconstruction using a geometrical con-  
745 struction. *Physical review A*, 45(6):3403, 1992.
- 746 [18] Eugene Tan, Shannon Algar, Débora Corrêa, Michael Small, Thomas Stemler,  
747 and David Walker. Selecting embedding delays: An overview of embedding  
748 techniques and a new method using persistent homology. *Chaos: An Interdis-  
749 ciplinary Journal of Nonlinear Science*, 33(3), 2023.
- 750 [19] Jennifer M Radin, Anthony W Hawksworth, Peter E Kammerer, Melinda Bal-  
751 ansay, Rema Raman, Suzanne P Lindsay, and Gary T Brice. Epidemiology  
752 of pathogen-specific respiratory infections among three US populations. *PLoS  
753 One*, 9(12):e114871, 2014.
- 754 [20] Guojian Lv, Limei Shi, Yi Liu, Xuecheng Sun, and Kai Mu. Epidemiological  
755 characteristics of common respiratory pathogens in children. *Scientific Reports*,  
756 14(1):16299, 2024.
- 757 [21] Saverio Caini, Adam Meijer, Marta C Nunes, Laetitia Henaff, Malaika Zounon,  
758 Bronke Boudewijns, Marco Del Riccio, and John Paget. Probable extinction of  
759 influenza b/yamagata and its public health implications: a systematic literature  
760 review and assessment of global surveillance databases. *The Lancet Microbe*,  
761 2024.

- 762 [22] Zhiyuan Chen, Joseph L-H Tsui, Bernardo Gutierrez, Simon Busch Moreno,  
763 Louis du Plessis, Xiaowei Deng, Jun Cai, Sumali Bajaj, Marc A Suchard,  
764 Oliver G Pybus, et al. COVID-19 pandemic interventions reshaped the global  
765 dispersal of seasonal influenza viruses. *Science*, 386(6722):eadq3003, 2024.
- 766 [23] Bryan T Grenfell, Ottar N Bjørnstad, and Bärbel F Finkenstädt. Dynamics of  
767 measles epidemics: scaling noise, determinism, and predictability with the TSIR  
768 model. *Ecological monographs*, 72(2):185–202, 2002.
- 769 [24] Samit Bhattacharyya, Per H Gesteland, Kent Korgenski, Ottar N Bjørnstad,  
770 and Frederick R Adler. Cross-immunity between strains explains the dynamical  
771 pattern of paramyxoviruses. *Proceedings of the National Academy of Sciences*,  
772 112(43):13396–13400, 2015.
- 773 [25] Virginia E Pitzer, Cécile Viboud, Vladimir J Alonso, Tanya Wilcox, C Jessica  
774 Metcalf, Claudia A Steiner, Amber K Haynes, and Bryan T Grenfell. Environmental  
775 drivers of the spatiotemporal dynamics of respiratory syncytial virus in  
776 the United States. *PLoS pathogens*, 11(1):e1004591, 2015.
- 777 [26] Katharine R Dean, Fabienne Krauer, Lars Walløe, Ole Christian Lingjærde, Barbara  
778 Bramanti, Nils Chr Stenseth, and Boris V Schmid. Human ectoparasites  
779 and the spread of plague in Europe during the Second Pandemic. *Proceedings  
780 of the National Academy of Sciences*, 115(6):1304–1309, 2018.
- 781 [27] Margarita Pons-Salort and Nicholas C Grassly. Serotype-specific immunity  
782 explains the incidence of diseases caused by human enteroviruses. *Science*,  
783 361(6404):800–803, 2018.
- 784 [28] Sarah Cobey and Edward B Baskerville. Limits to causal inference with state-  
785 space reconstruction for infectious disease. *PloS one*, 11(12):e0169050, 2016.
- 786 [29] Public Health Agency of Canada. Respiratory virus detections in  
787 Canada. 2024. <https://www.canada.ca/en/public-health/services/surveillance/respiratory-virus-detections-canada.html>. Accessed Sep  
788 4, 2024.
- 789 [30] Centre for Health Protection. Detection of pathogens from respiratory  
790 specimens. 2024. <https://www.canada.ca/en/public-health/services/surveillance/respiratory-virus-detections-canada.html>. Accessed Nov  
791 20, 2024.
- 792 [31] Korea Disease Control and Prevention Agency. Acute respiratory infection,  
793 Sentinel surveillance infectious diseases. 2024. <https://dportal.kdca.go.kr/pot/is/st/ari.do>. Accessed Nov 20, 2024.

- 797 [32] Edward Goldstein, Sarah Cobey, Saki Takahashi, Joel C Miller, and Marc Lip-  
798 sitch. Predicting the epidemic sizes of influenza A/H1N1, A/H3N2, and B: a  
799 statistical method. *PLoS medicine*, 8(7):e1001051, 2011.
- 800 [33] Bob Carpenter, Andrew Gelman, Matthew D Hoffman, Daniel Lee, Ben  
801 Goodrich, Michael Betancourt, Marcus A Brubaker, Jiqiang Guo, Peter Li,  
802 and Allen Riddell. Stan: A probabilistic programming language. *Journal of*  
803 *statistical software*, 76, 2017.
- 804 [34] Stan Development Team. RStan: the R interface to Stan, 2024. R package  
805 version 2.32.6.